

Authors' response to comments and suggestions from referees and the editor

Black, italic: Referee's comments

Blue: Author's reply

Red: Changes in the original discussion paper

5

1. in the manuscript, you state in line 289 that "the NO₂ sources in Feicheng are mainly related to traffic and concentrated along the S104". I frankly cannot see that in the figure and suggest to remove this statement.

Removed.

10

2. in the caption of Figure 10, you write "NO₂ emission". Please replace by "NO_x emission" as emissions are usually in the form of NO, not NO₂.

Replaced NO₂ emission with NO_x emission.

15

3. when introducing the car-DOAS measurements, please add that the retrieval window in the UV differs from the one used for the airborne observations.

We added this statement in line 338.

20

It is worth noting that the retrieval window in the mobile DOAS observations differs from the one used for the airbrine observations.

4. please add acknowledgements and data sources for TROPOMI and LANDSAT 8 data.

25

We added acknowledgements and data sources for TROPOMI and LANDSAT 8 data.

Acknowledgments. We would like to thank Thomas Danckaert, Caroline Fayt and Michel Van Roozendael for help on QDOAS software. We are thankful to the following agencies for providing the satellite data: The Sentinel 5 Precursor TROPOMI Level 2 NO₂ product is developed by KNMI with funding from the Netherlands Space Office (NSO) and processed with funding from the European Space Agency (ESA). TROPOMI data can be downloaded from <https://s5phub.copernicus.eu>. Landsat 8 OLI data have been produced, archived, and distributed by the U.S. Geological Survey (USGS). The original Landsat surface reflectance algorithm was developed by Dr. Eric Vermote, NASA Goddard Space Flight Center (GSFC). Landsat 8 OLI data are available at <https://earthexplorer.usgs.gov/>.

35

5. in the introduction, it would be good to also make reference to some other imaging DOAS instruments that have been flown for NO₂ measurements:

We added these references of other imaging DOAS instruments in section 1.

40

For the purpose of retrieval of urban NO₂ horizontal distribution, Popp et al. (2012), General et al. (2014), Schönhardt et al. (2015), Lawrence et al. (2015), Nowlan et al. (2016), and Lamsal et al. (2017) performed their measurements separately in Zürich, Switzerland, Indianapolis and Barrow, USA, Ibbenbüren, Germany, Leicester, England, Houston, USA, and Maryland, USA.

45

Lamsal, L. N., S. J. Janz, N. A. Krotkov, K. E. Pickering, R. J. D. Spurr, M. G. Kowalewski, C. P. Loughner, J. H. Crawford, W. H. Swartz, and J. R. Herman (2017), High-resolution NO₂ observations from the Airborne Compact Atmospheric Mapper: Retrieval and validation, *J. Geophys. Res. Atmos.*, 122, 1953–1970, doi:10.1002/2016JD025483.

50 Nowlan, C. R., Liu, X., Leitch, J. W., Chance, K., González Abad, G., Liu, C., Zoogman, P., Cole, J., Delker, T., Good, W., Murcray, F., Ruppert, L., Soo, D., Follette-Cook, M. B., Janz, S. J., Kowalewski, M. G., Loughner, C. P., Pickering, K. E., Herman, J. R., Beaver, M. R., Long, R. W., Szykman, J. J., Judd, L. M., Kelley, P., Luke, W. T., Ren, X., and Al-Saadi, J. A.: Nitrogen dioxide observations from the Geostationary Trace gas and Aerosol Sensor Optimization (GeoTASO) airborne instrument: Retrieval algorithm and measurements during DISCOVER-AQ Texas 2013, *Atmos. Meas. Tech.*, 9, 2647–2668,
55 <https://doi.org/10.5194/amt-9-2647-2016>, 2016.

Schönhardt, A., Altube, P., Gerilowski, K., Krautwurst, S., Hartmann, J., Meier, A. C., Richter, A., and Burrows, J. P.: A wide field-of-view imaging DOAS instrument for two-dimensional trace gas mapping from aircraft, *Atmos. Meas. Tech.*, 8, 5113–5131, doi:10.5194/amt-8-5113-2015, 2015.

60

General, S., Pöhler, D., Sihler, H., Bobrowski, N., Frieß, U., Zielcke, J., Horbanski, M., Shepson, P. B., Stirn, B. H., Simpson, W. R., Weber, K., Fischer, C. and Platt, U.: The Heidelberg Airborne Imaging DOAS Instrument (HAIDI) – a novel imaging DOAS device for 2-D and 3-D imaging of trace gases and aerosols, *Atmos. Meas. Tech.*, 7(10), 3459–3485, doi:10.5194/amt-7-3459-2014, 2014.

65

6. Line 133: Can the authors quantify in the text the radiance threshold applied?

70

We used a radiance threshold of $12.8 \mu\text{W}\cdot\text{cm}^{-2}\cdot\text{sr}^{-1}\cdot\text{nm}^{-1}$ at 450 nm.

Furthermore, a radiance threshold of $12.8 \mu\text{W}\cdot\text{cm}^{-2}\cdot\text{sr}^{-1}\cdot\text{nm}^{-1}$ at 450 nm is set to neglect some over-illuminated ground pixels inside the flight area, which are usually caused by the presence of clouds or water mirror reflection.

75

7. Equation 1 is valid for a total VCD, but not tropospheric VCD as is referred to below this equation. The stratospheric slant column must also be subtracted from the dSCD. In lines Line 167-170, it is stated that the stratospheric column cancels out during flight from the reference but in the comment back to the reviewers it was quantified as a difference up to $8e14$ due to the changes in the slant path through the atmosphere, which is not stated in the text. This is an impact and should either
80 be added to this product or by quantified in the error estimate. It is a change of 23% over the time period of the flight...

We added this stratospheric correction in Sect 4.2.

85 Changes in the stratospheric NO_2 could also propagate to the measured tropospheric columns of UVHIS. Under the assumption of a constant stratosphere in time and space during the flight, the changes in the SZA impact the column difference between the measurement and the reference. To correct the change in the stratospheric NO_2 SCD, we apply a geometric approximation of the stratospheric AMF with a stratospheric VCD of 3.5×10^{15} molec cm^{-2} from TROPOMI product. The maximum change in the stratospheric SCD with respect to the reference, was 8×10^{14} molec cm^{-2} .

90 8. Line 195: State the range of AOD measurements from MODIS for this flight day.

The MODIS AODs in the flight area range from 0.142 to 0.365.

95 9. Line 228: Inconsistencies are expected because one is radiance and the other is surface reflectance. They aren't the same thing thought they should be similar in spatial pattern. I don't see differences that would be caused by time differences with how it is displayed here. The one detail that does stick out though is that roadway isn't visible in the radiance measurements even though UVHIS should be higher resolution than Landsat, so can this be explained just by the color bar range choice? Perhaps but the unweighted averaging within the grid as discussed in Section 4.4? It would be nice to have a sentence or two about this.

100

Actually, the roadway is visible in Fig. 9 (a), but the width of the road looks thinner compared to Fig. 9 (b). We replaced this figure with a higher resolution one. We modified the last sentence in this paragraph.

105 Fig. 9 also shows several slight inconsistencies between the UVHIS measured radiance and the Landsat 8 surface reflectance product. For example, the east-west main road looks thinner in Fig. 7 (a) compared to Figs. 7 (b) and (c). This could be explained by the relatively higher spatial resolution performance of the UVHIS and the resampling of Landsat 8 pixels.

10. Line 278: *The authors refer to this ‘weaker’ plume, but it has a higher column density than the last described plume.*

110 We deleted the word ‘weaker’.

11. *Is the noise in Figure 11 primarily attributable to surface reflectivity?*

115 We thought the noise in Fig. 11 is primarily attributable to random noise, because the spatial patterns of VCD and surface reflectance (or radiance) are inconsistent.

12. Line 297: *This is not correct. Areas with NO₂ sources can vary dramatically with time. This is a sample size of 2. Emissions from sources aren’t always constant and their footprints can change dramatically due to meteorology as well. In the case of region B, the variability is almost just as large as it is in region a (maybe even more so). The only consistent region is region C.*

120

We agreed this correction and modified the last few sentences in this paragraph.

125 In these three regions, only region C is temporally consistent with relatively low NO₂ columns, whilst a large temporal variety of NO₂ VCDs exists in region A and region B because of inconstant emission sources and changing meteorology.

13. Line 315: *The authors refer to AMF of 2 and AMF of 1.8 for the reference in the same sentence for the reference. This is confusing. I think we need the AMF for TROPOMI in this case to convert 1e15 VCD to its SCD then divide by the AMF from UVHIS.*

130

We thought the TROPOMI AMF of the reference may be inappropriate considering the different viewing angles. The AMF of 1.8 is near the mean value of the UVHIS AMFs in the reference area, and the AMF of 2.0 is near the mean value of all UVHIS AMFs.

135 *14. Line 365: This comment is in relation to the low bias by UVHIS and high bias by mobile DOAS. It seems that the mobile*
DOAS would probably be more sensitive to near surface pollution than the aircraft. Is the assumption of the a priori profile
a reason for the aircraft being lower than the mobile DOAS and is there an optimal profile between the two that would result
in the two being closer to 1:1. I am not suggesting to redo all work with a new a priori but perhaps doing the sensitivity test
140 *like was done on the airborne work on the mobile DOAS and see if that is a plausible cause for the biases. Then reflect on*
that in the text.

We did a sensitivity test, the detail is in next answer.

15. Last sentence in Section 6: We haven't been given reason to believe that the spatial footprint of the mobile DOAS is
145 *smaller than the UVHIS pixels. Therefore, this sentence is not a valid reason for these results. The above comment seems*
more plausible.

We deleted this sentence and modified to

150 *A sensitivity test of the AMF on the NO₂ profile was performed for all co-located measurements, using a box profile of 500*
m. Compared to the box profile of 2 km, the UVHIS AMFs decreased by an average of 17 %, whilst the mobile DOAS
AMFS decreased by an average of 2.7 %. This results suggest that a more realistic profile with the NO₂ layer closer to the
ground could improve the slope closer to unity.

155 *16. Line 20 + final paragraph in Section 6: It is nice to see this improvement in the correlation between Fig 14 a and b. Is*
the correlation different because of the time difference between measurements or because of the location near the steel
factory? It seems more likely to focus on is the difference in time between measurements in the text rather than focusing on
the location near the steel plant. This should be detailed in the caption of Figure 14 as well.

160 We added the time difference information in the caption of Fig. 14.

17. Title has a misspelled word: Imaing = imaging

Fixed

165

18. Line 44: Change 'lower' to 'coarser'

Fixed

170 *19. Delete Lines 120-122. These details are on the next page and fit better there.*

Deleted

175 *20. Line 215: Delete Other RTM parameters used in the AMF calculations are also provided in Fig. 7. Because there are no other parameters shown that I can see.*

Deleted

180 *21. Line 236: 'estimated' PBL height.*

Fixed

185 *22. Should section 4.4 go before 4.3 or even before 4.1 because geolocation and other steps would have to be performed before AMF analysis to link it to surface reflectivity and other attitude parameters?*

We added a geo-referencing part in Sect 4.1 and changed the title of Sect 4.4 to 'Resampling and mapping'.

23. Line 264: refer to Figure 10.

190 We added 'As shown in Fig. 10' in this sentence.

24. Line 310: the mobile DOAS system hasn't been introduced yet so it seems inappropriate to bring up here.

Deleted

195 *25. Table 3 and Table 5: In the text, please explain what the intensity offset is.*

This is the offset parameter in the DOAS fitting for possible instrumental and/or atmospheric stray light or residual dark current signal. We changed the 'Intensity offset' to 'Offset' to reduce misunderstandings.

200

26. Figure 4, 10, 12, and 13: Please make the numbers indicating the point sources larger. They're hard to read.

We updated these figures.

205 *27. The authors included water vapour in the DOAS analysis, unfortunately this did not improve the fit. Nevertheless the water cross section should be added in Table 5.*

In the manuscript, Table 5 lists the parameters of mobile DOAS system. We did not add a water vapour cross section because the absorption of water vapour is weak in the 356-376 nm fit window of the mobile DOAS.

210

215

220

225

230

Relevant changes:

235

1. Modified the title.
2. Modified the affiliation.
3. Added a stratospheric correction in the DOAS analysis.
4. Added a sensitivity test of the AMF on the NO₂ profile for the co-located measurements.

240

5. Updated Figs. 4, 9, 10, 12, 13.

6. Fixed grammatical problems in the text.

245

250

255

260

265

~~The first~~**First** high-resolution tropospheric NO₂ observations from the Ultraviolet Visible Hyperspectral ~~Imaing~~**Imaging** Spectrometer (UVHIS)

270

Liang Xi ^{1,2}, Fuqi Si ¹, Yu Jiang ¹, Haijin Zhou ¹, Kai Zhan ¹, Zhen Chang ¹, Xiaohan Qiu ¹ and Dongshang Yang ^{1,2}

¹Key Laboratory of Environmental Optics and Technology, Anhui Institute of Optics and Fine Mechanics, Chinese Academy of Sciences, Hefei 230031, China

275 ²[Science Island Branch of Graduate School](#), University of Science and Technology of China, Hefei, 230026, [Anhui](#), China

Correspondence to: Fuqi Si (sifuqi@aiofm.ac.cn)

280

285

290

Abstract. We present a novel airborne imaging differential optical absorption spectroscopy (DOAS) instrument: Ultraviolet Visible Hyperspectral Imaging Spectrometer (UVHIS), which is developed for trace gas monitoring and pollution mapping. Within a broad spectral range ~~from of~~ 200 to 500 nm, ~~operated and operating~~ in three channels, the spectral resolution of UVHIS is better than 0.5 nm. The optical design of each channel comprises a fore-optics with a field of view (FOV) of 40°, an Offner imaging spectrometer, and a charge-coupled device (CCD) array detector of 1032 × 1072 pixels. A first demonstration flight using UVHIS was ~~undertaken conducted~~ on 23 June 2018, above an ~~area of~~ approximate 600 km² ~~area~~ in Feicheng, China, with a spatial resolution of about 25 × 22 m². Measurements of nadir backscattered solar radiation of channel 3 are used to retrieve tropospheric vertical column densities (VCDs) of NO₂ with a mean total error of 3.0 × 10¹⁵ molec cm⁻². The UVHIS instrument clearly detected several emission plumes transporting from south to north, with a peak value of 3 × 10¹⁶ molec cm⁻² in the dominant one. ~~The~~ UVHIS NO₂ vertical columns are ~~well correlated consistent~~ with ~~the~~ ground-based mobile DOAS observations, with a correlation coefficient of 0.65 for all co-located measurements, a correlation coefficient of 0.86 for ~~the~~ co-located measurements that only circled the steel factory, and a slight underestimation for ~~the~~ polluted observations. This study demonstrates the capability of UVHIS for NO₂ local emission and transmission monitoring.

1 Introduction

295

Nitrogen oxides (NO_x), the sum of nitrogen monoxide (NO) and nitrogen dioxide (NO₂), ~~plays play~~ a key role in the chemistry of the atmosphere, such as the ozone destruction in the stratosphere (Solomon, 1999), and the secondary aerosol formation in the troposphere (Seinfeld and Pandis, 2016). In the troposphere, despite lightning, soil emissions and other natural processes, the main sources of NO_x are anthropogenic activities like fossil fuel combustion by power plants, factories, and road transportation, especially in ~~the~~ urban and polluted regions. As an indicator of anthropogenic pollution which leads to negative effects both on the environment and human health, the amounts and spatial distributions of NO_x ~~attract large~~ have attracted significant attention. For example, China ~~becomes has become~~ one of the largest NO_x emitters in

the world due to ~~its~~ fast ~~industrialization~~~~industrialisation~~, meanwhile China ~~is~~~~has~~ also ~~experiencing~~~~experienced~~ a series of
300 severe air pollution problems in recent years (Crippa et al., 2018; An et al., 2019). Therefore, ~~measuring~~ ~~the~~ NO_x distribution
by ~~application of~~~~applying~~ different techniques, would benefit the pollutant emission detection and the air quality trend
forecast (Liu et al., 2017; Zhang et al., 2019).

Compared to NO, Nitrogen dioxide (NO₂) is more stable in the atmosphere. Based on the characteristic absorption structures
of NO₂ in the ultraviolet-visible spectral range, the differential optical absorption spectroscopy (DOAS) technique has been
305 applied to retrieve ~~the~~ light path integrated densities from different platforms (Platt and Stutz, 2008). ~~Combining~~~~Combined~~
the imaging spectroscopy technique, imaging DOAS instruments were developed in recent years to determine the ~~trace gases~~
temporal variation ~~as well as~~~~and~~ the two dimensional distribution ~~of trace gases~~. ~~The~~~~Global~~~~global~~ horizontal distribution of
tropospheric NO₂ and other trace gases has been mapped and studied by several space-borne sensors, including
SCIAMACHY (Scanning Imaging Absorption Spectrometer for Atmospheric CHartographY; Bovensmann et al., 1999),
310 GOME (Global Ozone Monitoring Experiment; Burrows et al., 1999), GOME-2 (Munro et al., 2016), OMI (Ozone
Monitoring Instrument; Levelt et al., 2006) and TROPOMI (TROPospheric Ozone Monitoring Instrument; Veefkind et al.,
2012). The Environmental trace gases Monitoring Instrument (~~EIMEMI~~; Zhao et al., 2018; Cheng et al., 2019; Zhang et al.,
2020), as the first designed space-borne trace gas sensor in China, was launched on 9 May 2018, on-board the Chinese
GaoFen-5 (GF5) satellite. ~~In terms of~~~~The~~ spatial resolution, ~~the majority of these of most~~ space-borne sensors ~~are~~~~is~~ ~~lower~~
315 ~~coarser~~ than 10 × 10 km², except ~~for that of~~ TROPOMI ~~with a relative higher resolution of which is~~ 3.5 × 5.5 km².

~~In order to~~~~To~~ achieve a spatial resolution higher than 100 × 100 m² ~~to investigate~~~~for investigating~~ the spatial distribution in
urban areas and individual source emissions, several researchers have applied ~~the~~ imaging DOAS instruments on airborne
platforms. The airborne imaging DOAS measurement was ~~firstly~~~~first~~ performed by Heue et al. (2008) over ~~the~~ South
African Highveld plateau. ~~For the purpose of retrieval of~~~~To retrieve~~ urban NO₂ horizontal distribution, Popp et al. (2012),
320 ~~General et al. (2014), Schönhardt et al. (2015), and~~ Lawrence et al. (2015), ~~Nowlan et al. (2016), and Lamsal et al. (2017)~~
~~performed their measurements separately~~~~respectively took measurements~~ in Zürich, Switzerland, ~~;~~ ~~Indianapolis and Barrow,~~
~~USA; Ibbenbüren, Germany; and~~ Leicester, England; ~~Houston, USA; and Maryland and Washington DC, USA~~. In 2013, an
airborne measurement focusing on source emissions was ~~performed~~~~taken~~ in China, over Tianjin, Tangshan and ~~the~~ Bohai
~~gulf~~ Bay (Liu et al., 2015). An inter-comparison study of four airborne imaging DOAS instruments over Berlin, Germany,
325 suggests a good agreement between different sensors, and the effectiveness of imaging DOAS ~~to reveal~~~~in revealing~~ the fine-
scale horizontal variability in tropospheric NO₂ in ~~an~~ urban context (Tack et al., 2019).

Here we present a novel airborne imaging DOAS instrument: Ultraviolet Visible Hyperspectral Imaging Spectrometer
(UVHIS), ~~which was~~ designed and developed by Anhui Institute of Optics and Fine Mechanics, Chinese Academy of
Sciences (AIOFM, CAS). As a hyperspectral imaging sensor with a high spectral and spatial resolution, UVHIS is designed
330 ~~to be operated~~~~for operation~~ on ~~an~~ aircraft platform for ~~the purpose of~~ atmospheric trace gas measurements and pollution
monitoring over large ~~area~~~~areas~~ in a relative short time frame. By using the DOAS technique and geo-referencing, ~~the~~ ~~two~~

~~two~~-dimensional spatial distribution of tropospheric NO₂ of its first demonstration flight over Feicheng, China is also presented in this paper.

~~This paper is organised as follows~~~~The organization of this paper is listed as follows:~~ ~~Seet-~~Section 2 presents a technical description of the UVHIS system, ~~as well as~~and its preflight calibration results. Section 3 introduces the detailed information of its first research flight ~~above-over~~ Feicheng, China. Section 4 describes the developed algorithm for the retrieval and geographical mapping of tropospheric NO₂ vertical column densities from hyperspectral data. Section 5 presents the retrieved NO₂ column densities, and Section 6 compares the airborne measurements with the correlative ground-based data sets from a mobile DOAS system.

340 **2 Instrument Details**

1.1 ~~The~~-UVHIS instrument

UVHIS is a hyperspectral instrument measuring nadir backscattered solar radiation in the ultraviolet and visible wavelength region from 200 to 500 nm. The instrument is operated in three channels with the wavelength ranges of 200-276 nm (channel 1), 276-380 nm (channel 2) and 380-500 nm (channel 3) for minimal stray light effects and highest spectral performance.

345 The main characteristics of UVHIS are ~~summarized~~summarised in Table 1.

Figure 1 shows the optical bench of channel 3 and ~~that those of~~ the other two are similar. The optical design of each channel comprises a telecentric fore-optics, an Offner imaging spectrometer, and a ~~two-two~~-dimensional ~~charge-coupled device~~ ~~(CCD)~~CCD array detector. The Offner imaging spectrometer consists of a concave mirror and a convex grating. The backscattered~~Backscattered~~ light below the aircraft is collected by a wide-field telescope with a FOV of 40° in the across-track dimension. After passing through a bandpass filter and a 12.5 mm long entrance slit in the focal plane, the light is reflected and diffracted by a concave mirror and a convex grating. The dispersed light is imaged onto a frame transfer CCD detector, which consists of 1032 × 1072 individual pixels. For the ~~purpose of~~ alignment and slight adjustment of the spectrometer, only the central 1000 rows of pixels are well illuminated in the across-track dimension. In the wavelength dimension, the image covers central 1024 columns of pixels on the CCD detector ~~while, whilst~~ the left and right edges are used to monitor dark current. The spectral sampling and spectral resolution of all three channels can be found in Table 1.

To reduce dark current and improve the signal-to-noise ratio (SNR) of the instrument, the CCD detector is thermally ~~stabilized~~stabilised at ~~-20~~°C with a temperature stability of ± 0.05°C (Zhang et al., 2017). However, the optical bench is not thermally controlled, because the instrument is mounted inside the aircraft platform which ~~is temperature consistent at~~has a constant temperature of 20 °C. The UVHIS is mounted on a Leica PAV-80 gyro-~~stabilized~~stabilised platform that provides angular motion compensation. A high-grade Applanix navigation system on-board is used to receive ~~the~~ position (i.e. latitude, longitude, and elevation) and orientation (i.e. pitch, roll, and heading) information, which ~~is-are~~ required for accurate geo-referencing. The UVHIS instrument telescope collects the solar radiation backscattered from the surface and

atmosphere through a fused silica window ~~on-at~~ the bottom of the aircraft. In the case of NO₂ measurement, all observations in this study only use ~~the~~ channel 3.

365 2.2 Preflight calibration

Spectral and radiometric calibration ~~in the laboratory were done~~ were performed in the laboratory prior to the flights to reduce errors in spectral analysis.

For radiometric calibration, we used an integrating sphere with a tungsten halogen lamp for channel 2 and channel 3. ~~While for~~ For channel 1, a diffuser plate with a Newport xenon lamp ~~is was~~ used for ~~a~~ sufficient ultraviolet output. With the help of a well-well-calibrated spectral radiometer to monitor the radiance of calibration system, the digital numbers (~~DNs~~) from the CCD detectors of the three channels can be converted to radiance correctly. ~~The uncertainty~~ Uncertainty of absolute radiance calibration of the UVHIS is 4.89 % for channel 1, 4.67 % for channel 2 and 4.42 % for channel 3.

~~The preflight~~ Preflight wavelength calibration was also performed in the laboratory, using a mercury–argon lamp and a ~~tunable~~ unable laser as light sources. We modelled the slit function of the UVHIS using a symmetric Gaussian function. Spectral registration and slit function calibration ~~are were~~ achieved by least square fitting of the characteristic lines in the collected spectra. Table 2 lists the retrieved full-width at half ~~maximums~~ maximum values (FWHMs) for channel 3. Figure 2 shows the measured slit functions at 450.504 nm for 9-nine viewing angles (i.e. -20°, -15°, -10°, -5°, 0°, 5°, 10°, 15°, 20°), and the respective retrieved slit function shapes using a symmetric Gaussian function. These Gaussian fit results suggest that a symmetric Gaussian function is a reasonable assumption for the slit shape in all viewing directions.

380 3 Research flight

The first demonstration flight ~~above-over~~ Feicheng ~~city~~ City, Shiheng ~~town~~ Town and neighbouring rural areas was ~~performed-conducted~~ on 23 June 2018, aiming at producing tropospheric NO₂ field maps of a large area in a relatively short time frame. Feicheng is a county-level city in Shandong province, ~~approximately~~ about 410 km away from Beijing. Figure 3 shows the TROPOMI NO₂ tropospheric observation on 23 June, 2018, with the background Google map and the location of Feicheng. The flight area is located on the south bank of the Yellow River, at the western foot of Mount Tai. The UVHIS was operated from the Y-5 aircraft at an altitude of 3 km above sea level, ~~which is~~ higher than the height of planetary boundary layer (PBL), with an average aircraft ground speed of 50 m/s. An overview of the observation area and the flight lines are provided in Fig. 4. The aircraft took off at local noon from the airfield in Pingyin ~~county~~ County, ~~approximately~~ about 19 km northwest of the centre of the field. An area of approximately 600 km² was covered in 3 ~~hourh~~, under clean sunny and cloudless conditions with low-speed southerly winds.

~~Research-The research~~ flight ~~consists-of~~ included 13 parallel lines in the east-west direction, starting from the lower left corner in Fig. 2. The distance between adjacent lines ~~is was~~ 1.5 km, ~~while-while~~ the swath width of each individual line ~~is about~~ was approximately 2.2 km. Gapless coverage between adjacent lines can be guaranteed in this pattern because of the

adequate overlap. To validate the NO₂ column densities retrieved from the UVHIS by comparison to ground measurements, mobile DOAS measurements were ~~performed-taken~~ inside the research area on the same day. As shown in Fig. 4, the measurements of the mobile DOAS system circled around the steel factory and the power plant, which are the presumed major emission sources inside the observation area.

~~In the condition of spatial binning by 10 pixels across track, the across track spatial resolution of the ground pixel is about 22 m. At typical aircraft ground speed of 50 m/s and integration time of 0.5 s, the along track spatial resolution of the ground pixel is about 25 m.~~

4 Data processing chain

The NO₂ tropospheric vertical column density (VCD) retrieval algorithm of the UVHIS consists of four major steps. First, some necessary ~~preprocessingpre-processing~~ procedures are required before any spectral analysis of the UVHIS data. Next, the UVHIS spectral data after ~~preprocessingpre-processing~~ are ~~analyzed-analysed~~ in a suitable wavelength region by ~~application-applying~~ of the well-established DOAS technique. ~~After that~~ Then, the air mass factors (AMFs) are calculated for every observation based on the SCIATRAN radiative transfer model to convert the slant column densities (SCDs) to tropospheric vertical column densities. In the final step, ~~the geo-referenced combining with sensor position and orientation information,~~ NO₂ VCDs are ~~geo-referencedresampled~~ and overlaid onto Google satellite map layers.

4.1 Pre-processing

The ~~preprocessingpre-processing~~ procedure before spectral analysis includes data selection, geo-referencing, dark current correction, spatial binning, and in-flight calibration. First, the spectral data acquired during ~~U-turns of~~ aircraft U-turns are removed in the processing because of the large and changing orientation angles. ~~Also Furthermore,~~ a ~~threshold of radiance values-radiance threshold of~~ $12.8 \mu\text{W cm}^{-2} \text{sr}^{-1} \text{nm}^{-1}$ at 450 nm is set to neglect some over-illuminated ground pixels inside the flight area, which are usually caused by the presence of clouds or water mirror reflection. During the entire flight, the sun glinted on water ~~occurred~~ several times in the southern part of the flight area, especially above the river near the reference area. However, cloud was not present due to the clean clear-sky weather condition.

Accurate geo referencing is essential for emission source locating and data comparison, and can be achieved with the sensor position and orientation information recorded by the navigation system and IMU on-board.

~~The dark~~ Dark current correction is performed based on the measurement at the start of the entire flight by blocking the fore-optics, which is necessary to improve the instrument performance and reduce the analysis error in DOAS fit.

In order to increase the SNR of the instrument and the sensitivity to NO₂, the raw pixels of the imaging DOAS are usually aggregated in the ~~across-track direction~~ and along-track directions. According to photon statistics when only shot noise is considered, the SNR should rise with the square root of the number of binned spectra. However, this improved SNR of the

instrument results ~~a reduction of in reduced~~ spatial resolution. In ~~the~~ data analysis of ~~the~~ Feicheng flight, we use ~~the~~ binning
425 of 10 pixels in ~~the~~ across-track direction, resulting in a ground pixel size of ~~about approximately~~ $25 \times 22 \text{ m}^2$.
~~Since Given that~~ the wavelength-to-pixel registration and the slit function shape of ~~the~~ UVHIS could change compared to
laboratory calibration results, in-flight wavelength calibration is essential for the next DOAS analysis. This in-flight
wavelength calibration is achieved by fitting the measured spectra to a high-resolution solar reference (Chance and Kurucz,
2010) with slit function convolution and wavelength shift. The nominal wavelength-to-pixel registration determined in
430 laboratory calibration, is used as initial values in the iteratively fitting procedure for convergence to the optimal solution. The
effective shifts and FWHMs of different across-track positions are plotted in Fig. 5. ~~Results The results~~ at three wavelengths
are ~~shown presented as follows~~: blue for 430 nm (the start of the analysis wavelength region), green for 450 nm (the middle
of the analysis wavelength region) and red for 470 nm (the end of the analysis wavelength region).

4.2 DOAS analysis

435 After ~~preprocessing pre-processing~~, the observed UVHIS spectra are analysed ~~by the application of using the~~ QDOAS
(Danckaert et al., 2020) software ~~in order~~ to retrieve ~~the~~ NO_2 slant column densities. The basic idea of the DOAS approach is
to separate broadband signals like surface reflectance and Rayleigh scattering, and narrow-band signals like trace gas
molecular absorption. The ~~fitting fit~~ window is ~~within 430 and 470 nm wavelength region~~, considered to contain strongly
structured NO_2 absorption features, and with low interference of other trace gases such as O_3 , O_4 , and water vapor. ~~The~~
440 ~~Absorption absorption~~ cross-sections of NO_2 and other trace gases and a synthetic Ring spectrum are simultaneously fitted to
the logarithm of the ratio of the observed spectrum ~~and to the~~ reference spectrum. These cross sections are made by
convolving the high-resolution cross sections with ~~the~~ in-flight wavelength calibration results for all across-track positions.
Further details of the DOAS analysis setting can be found in Table 3.

For each analysed spectrum, the direct result of the DOAS fit is ~~the~~ differential slant column density (dSCD), which is the
445 ~~difference of~~ NO_2 integrated concentration ~~difference~~ along the effective light path between the studied spectrum and the
selected reference spectrum (SCD_{ref}). Reference spectra were acquired over a clean rural area upwind of the urban and
factory areas, in the lower left corner of Fig. 4. In the quite homogeneous background area, several spectra were averaged to
increase the SNR of the reference spectrum. ~~For the purpose of avoiding To avoid~~ across-track biases, a reference spectrum is
required for each across-track position because of its intrinsic spectral response. ~~Under the assumption that the spatial and~~
450 ~~temporal variability of the stratospheric NO_2 field is negligible during the test flight, this approach eliminates the~~
~~stratospheric NO_2 contribution, making the results only sensitive to the tropospheric portion.~~ According to TROPOMI
tropospheric NO_2 product of ~~the~~ reference area on the same day, the residual NO_2 amount in the background spectra is
estimated to be $3 \times 10^{15} \text{ molec cm}^{-2}$. ~~Changes in the stratospheric NO_2 could also propagate to the measured tropospheric~~
~~columns of UVHIS. Under the assumption of a constant stratosphere in time and space during the flight, the changes in the~~
455 ~~SZA impact the column difference between the measurement and the reference. To correct the change in the stratospheric~~
 ~~NO_2 SCD, we apply a geometric approximation of the stratospheric AMF with a stratospheric VCD of $3.5 \times 10^{15} \text{ molec cm}^{-2}$~~

from TROPOMI product. The maximum change in the stratospheric SCD with respect to the reference, was 8×10^{14} molec cm^{-2} .

460 A sample NO_2 DOAS fit result and ~~the~~ corresponding residual of UVHIS spectra ~~is-are~~ illustrated in Fig. 6, with a differential slant column density (~~dSCD~~)~~dSCD~~ of $4.95 \pm 0.34 \times 10^{16}$ molec cm^{-2} and a RMS on the residuals of 4.27×10^{-3} .

4.3 Air mass factor calculations

465 SCD is the integrated concentration along the effective light path of observation, which is strongly dependent on the viewing geometry and the properties that influence radiative transfer of light through the atmosphere. VCD is the integrated concentration along a single vertical transect from the Earth's surface to the top of the atmosphere, which is independent of ~~the~~ changes in the light path length of ~~the~~ SCD.

$$\text{VCD}_i^t = \frac{\text{dSCD}_i + \text{dSCD}_i^s + \text{SCD}_{\text{ref}}^t}{\text{AMF}_i^t} = \frac{\text{dSCD}_i + \text{dSCD}_i^s + \text{VCD}_{\text{ref}}^t \times \text{AMF}_{\text{ref}}^t}{\text{AMF}_i^t}. \quad (1)$$

As shown in Eq. (1), ~~the dSCD~~, ~~dSCD~~_i from the DOAS fit can be converted to tropospheric ~~VCD~~_i, ~~VCD~~_i^t by dividing the ~~AMF~~_i, ~~AMF~~_i^t -which accounts for ~~the~~ enhancements in the light path (Solomon et al., 1987). ~~The dSCD~~_i^s ~~is the stratospheric SCD difference between the measurement and the reference, the~~ ~~SCD~~_{ref}^t, ~~the~~ ~~VCD~~_{ref}^t ~~and the~~ ~~AMF~~_{ref}^t ~~are the tropospheric SCD, VCD and AMF of the reference.~~ In this study, tropospheric NO_2 AMFs have been computed using the SCIATRAN (Rozaanov et al., 2014) radiative transfer model (RTM). ~~The~~ SCIATRAN model numerically calculates AMFs based on a priori information on the parameters that change ~~the~~ effective light path, such as sun and viewing geometry, trace gas and aerosol vertical profiles, ~~and~~ surface reflectance.

4.3.1 Parameters in RTM

475 (1) During ~~the~~ flight, ~~the~~ viewing geometry is retrieved from the orientation information of the aircraft. ~~Solar~~ ~~The solar~~ position defined by the solar zenith angle (SZA) and ~~the~~ solar azimuth angle (SAA), as well as ~~the~~ relative azimuth angle (RAA) can be calculated, based on the time information, ~~and the~~ latitude and longitude position of each observation. (2) Since the flight is performed under ~~a~~ clear-sky condition, the effect of cloud presence can be ~~neglected-ignored~~ in AMF computation. (3) ~~Surface~~ ~~The surface~~ reflectance used in AMF calculation is the product of the Landsat 8 Operational Land
480 Imager (OLI) space-borne instrument (Barsi et al., 2014). ~~Coastal~~ ~~The coastal~~ aerosol band (433 to 450 nm) is selected because its bandwidth is relatively narrow, and this band is basically inside the DOAS fitting window (Vermote et al., 2016). (4) Since no accurate trace gas vertical profile is available during ~~the~~ flight, a well-mixed vertical distribution (box profile) of NO_2 in the PBL is assumed. However, accurate PBL height is also unavailable, ~~a-so~~ ~~the~~ typical height of 2 km is a reasonable guess in ~~the case of a~~ sunny summer day in ~~the~~ mid-latitude area in China. (5) ~~Aerosol optical Depth~~ ~~The aerosol~~
485 ~~optical depth~~ (AOD) information used in AMF calculation is ~~the~~ MODIS AOD product MYD04 at 470 nm on the same day

with resampling for every ground UVHIS pixel (Remer et al., 2005), because ~~neither~~ ground-based aerosol measurement is ~~not performed, nor any and no~~ AERONET station data near the flight area ~~are is~~ available. The MODIS AOD measurements inside the flight area ranges from 0.14 to 0.36. Like the NO₂ profile, the aerosol extinction box profile is constructed from the PBL height and the AOD. ~~Single-A single~~ scattering albedo (SSA) is assumed to be 0.93, and an asymmetry factor is assumed to be 0.68 for aerosol extinction profile, based on previous studies of typical urban/industrial aerosols (Li et al., 2018).

The Landsat 8 surface reflectance is retrieved through atmospheric correction, using the Second Simulation of the Satellite Signal in the Solar Spectrum Vectorial (6SV) model (Vermote et al., 1997). Since ~~there is~~ no overpass on the same day existed inside the UVHIS research flight area, we ~~choose-selected the~~ surface reflectance product on 3 May 2018, considering the sunny weather condition and no cloud presence. The spatial resolution of Landsat is ~~about approximately~~ 30 m, which is slightly larger than that of the UVHIS. A resampling of the Landsat 8 surface reflectance product based on nearest neighbour interpolation ~~is-was~~ performed for every UVHIS ground pixel.

The radiative transfer equation in SCIATRAN is solved in a pseudo-spherical multiple scattering atmosphere, using the scalar discrete ordinate technique. Simulations ~~are-were~~ performed for the sensor altitude of 3 km above sea level, and the wavelength of the middle of the NO₂ fitting windows, i.e. 450 nm. A NO₂ AMF look-up table (LUT) was computed, with the different RTM parameter settings provided in Table 4. For each retrieved dSCD, an AMF was ~~linear-linearly~~ interpolated from the LUT based on the sun geometry, the viewing geometry, and the surface reflectance.

4.3.2 RTM dependence study

1. AMF dependence on the surface reflectance

As shown in Fig. 7, a time series of computed AMFs are plotted for the research flight on 23 June 2018, as well as the corresponding surface reflectance, solar zenith angles, and relative azimuth angles. ~~Other RTM parameters used in the AMF calculations are also provided in Fig. 7.~~ Note that only data of nadir observations are plotted for a ~~clearer-clear~~ display, and the time gaps between adjacent flight lines can be observed. Despite the ~~greater-great~~ degree of varieties in viewing and sun geometries, ~~it is obvious that~~ the AMFs strongly depend on the surface reflectance. Previous studies reported ~~in-by~~ Lawrence et al. (2015), Meier et al. (2017) and Tack et al. (2017) suggest a similar conclusion. A sensitivity test was carried out to investigate the impact of surface reflectance on the AMF calculations, based on the SCIATRAN model, with varying values of surface reflectance, and the fixed values of other parameters. ~~Results-The results~~ of this test are shown in Fig. 8 (a), and indicate that the relation between the surface reflectance and the AMF is non-linear. Especially when the surface reflectance is ~~blow-below~~ 0.1, the AMF increase with the surface reflectance rapidly.

Generally speaking, the AMF should be higher in the case of a bright surface reflectance, because more sunlight is reflected from the ground back to the atmosphere and then recorded by the airborne sensor. Compared to rural areas, urban and

520 industrial areas usually exhibit ~~an enhancement in value of~~enhanced surface reflectance and ~~subsequently a subsequent~~ increment ~~of in~~ AMF. As shown in Fig. 9, the dependency of the AMF on the surface reflectance is very strong. ~~Also~~ ~~Moreover,~~ a strong variability of ~~the~~ surface reflectance and ~~the~~ AMF can be observed in these areas. ~~From Fig. 9, we can~~ ~~also observe several slight inconsistencies between UVHIS measured radiance and Landsat 8 surface reflectance product,~~ ~~due to time offset and spatial resolution difference.~~Fig. 9 also shows several slight inconsistencies between the UVHIS measured radiance and the Landsat 8 surface reflectance product. For example, the east-west main road looks thinner in Fig. 7 (a) compared to Figs. 7 (b) and (c). This could be explained by the relatively higher spatial resolution performance of the UVHIS and the resampling of Landsat 8 pixels.

525 2. AMF dependence on profiles

Based on airborne UVHIS retrieval product, the horizontal distribution of NO₂ can be detected, but the vertical distribution of NO₂ in the atmosphere is ~~not available~~unavailable. The assumptions we made for ~~the~~ profile shape of ~~the~~ trace gas and aerosol extinction do not consider the effective variability during research flight, which can be expected in an urban area. Focusing on the impact of different profile shapes on the AMF computation, sensitivity tests of two different NO₂ profiles which are closer to ground surface ~~are were~~ performed: well-mixed NO₂ box profiles of 0.5 and 1 km heights. Compared to the box profile of 2 km which is ~~close to~~near the ~~estimated~~ height of PBL, ~~the~~ AMFs decreased by an average of 13 % in the case of a ~~box~~ profile of 1.0 km, ~~while whilst the~~ AMFs decreased by an average of 22 % in the case of a box profile of 0.5 km.

535 Depending on the relative position of ~~the~~ aerosol and trace gas layer, the optical thickness and ~~the~~ scattering properties, aerosols can enhance or reduce the AMF in different ways (Meier et al., 2017). If an aerosol layer is located above the majority of the trace gas, ~~the~~ aerosols with high SSA have a shielding effect as less scatter light passes through the trace gas layer, leading to a shorter light path. On the other hand, if aerosols and the trace gas are present in the same layer, ~~the~~ aerosols can lead to multiple scattering effects which extend the light path and result ~~in~~ a larger AMF. According to the simulations of a well-mixed aerosol box profile of 2 km and a pure Rayleigh atmosphere, AMFs are slightly higher (~~about by~~ ~~approximately~~ 1 %) ~~compared to~~than those of the pure Rayleigh scenario.

540 3. AMF dependence on sun and viewing geometries

~~As can be seen in Fig. 7,~~Figure 7 shows that the effect of sun and viewing geometries on AMFs is very small. Based on a previous study ~~from by~~ Tack et al. (2017), ~~the~~ changing SZA have the greatest effect on ~~the~~ AMFs, ~~in comparison~~compared to other sun and viewing geometries. In this study, we also ~~did performed~~ an AMF dependence analysis on SZAs and VZAs. 545 The SZA ~~varies varied~~ from 12.8° to 37.4° during the 3 ~~hour h~~ research flight, ~~while whilst~~ the VZA ~~ranges ranged~~ from 0° to 30° in most cases. As shown in Figs. 8 (b) and (c), the changes ~~of in~~ AMF ~~are were~~ less than 10% and 7% respectively, when other parameters ~~are were~~ set ~~as to the~~ mean ~~values~~. Generally, a larger SZA or a larger VZA could result ~~in~~ a longer light path through the atmosphere and thus a larger AMF.

4. AMF dependence on the analysis wavelength

550 The dependence of AMF on ~~the~~ analysis wavelength is shown in Fig. 9~~,~~. The AMF increases with the analysis wavelength. This could be explained by ~~the~~ Rayleigh scattering characteristics. ~~That is,~~ photons at shorter wavelengths are more likely to be scattered than photons at longer wavelengths, leading to ~~the~~ reduced sensitivity to AMF at shorter wavelengths. In the DOAS analysis wavelength window of 430-470 nm, the increase in AMF is ~~about~~ approximately 2 %.

4.4 ~~Geo-referencing~~ Resampling and mapping

555 ~~Accurate geo-referencing is essential for emission source locating and data comparison, and can be achieved with sensor position and orientation information recorded by navigation system and IMU on board. After geo-referencing, the~~ The geo-referenced NO₂ VCDs are gridded to combine overlapped adjacent measurements, with a spatial resolution of $0.0003^\circ \times 0.0002^\circ$. Corresponding to $27 \times 22 \text{ m}^2$, the grid size used is slightly larger than the effective spatial resolution of the UVHIS ~~for the purpose of reducing to reduce~~ the number of empty grid cells. All VCDs are assigned to a grid cell based on its centre
560 coordinates, and several VCDs in one grid cell are unweighted averaged. ~~As shown in Fig. 10, the~~ The final NO₂ VCD distribution map is plotted over ~~the~~ satellite ~~Maps-maps~~ layers in QGIS 3.8 software (QGIS development team, 2020).

5 Results

The tropospheric NO₂ VCD two-dimensional distribution map is shown in Fig. 10 for the research flight on 23 June 2018. With ~~a~~ the high performance of UVHIS in spectral and spatial resolution, ~~Figure 10~~ Fig. 10 shows fine-scale NO₂ spatial
565 variability to resolve individual emission sources. In general, the NO₂ distribution is dominated by several exhaust plumes with enhanced NO₂ concentration in the northwest part, ~~which~~ that share a transportation pattern from south to north ~~that is~~ consistent with the wind direction. These sources include a power plant, a steel factory, two cement factories, and several carbon factories. The largest plume with peak values of up to $3 \times 10^{16} \text{ molec cm}^{-2}$, ~~originates~~ originated from an emitter inside a steel factory (number 3 in Fig. 10). This dominant plume reaches its peak value outside at a small valley ~~about~~
570 approximately 1 km north of the factory, and ~~is~~ was transporting at least 9 km and seems to be continuing outside the flight region. This enhanced level of NO₂ may be caused by ~~the~~ terrain factor which contributes to the accumulation of pollution gases.

Numbers 4 to 6 represent other emitters inside the steel factory. ~~While, whilst~~ the exhaust plumes ~~originated~~ originated from numbers 4 and 5 merged with the dominant plume, the plume from number 6 ~~transports~~ transported to north individually with a peak
575 value of $1.4 \times 10^{16} \text{ molec cm}^{-2}$. A ~~weaker~~ plume with peak values of $1.5 \times 10^{16} \text{ molec cm}^{-2}$ ~~is~~ was also detected by UVHIS, which ~~seems~~ seemed to originate from the power plant. Indicated by number 2 in Fig. 10, this power plant is less than 2 km south of the steel factory. Number 1 in Fig. 10 indicates several carbon factories, which are located on the left side of the flight area. Several plumes with peak values of ~~1.5~~ 1.6 $\times 10^{16} \text{ molec cm}^{-2}$, gradually merged ~~together~~ during transportation

downwind. Numbers 7 and ~~Number~~8 in Fig. 10 represent two different cement factories. ~~Peak~~The peak values of these two
580 plumes are 1.5×10^{16} ~~molec cm⁻²~~ and 1.4×10^{16} molec cm⁻² respectively.

Compared to the industrial areas mentioned above, the pollution levels of the rural areas are much lower due to the lack of
contributing sources, ranging from 2 to 6×10^{15} molec cm⁻². The urban area of Feicheng ~~city~~City is located on the right side
of the flight area. Figure 11 is an enlarged map of the UVHIS NO₂ observations over Feicheng ~~city~~City, with a colour
that only extends to 7×10^{15} molec cm⁻². ~~Two~~The two black lines in Fig. 11 represent the truck roads in this city. ~~The~~S104
585 is a provincial highway that crosses Feicheng from north to south, ~~while the~~whilst S330 crosses Feicheng from east to west.
~~Although lots of noise can be observed in Fig. 11, the NO₂ sources in Feicheng are mainly related to traffic and concentrated
along the S104.~~

Due to temporal discontinuity of the flight lines and the dynamic characteristics of the tropospheric NO₂ field, artefacts can
be observed between adjacent flight lines. Figure 12 shows three flight lines that pass through the steel factory; at local times
590 of 13:26 (a), 13:32 (c), and 14:57 (b). Panels (a) and (b) represent the flight lines that cover the same area with a 1.5 ~~hour~~h
time gap, and panels (a) and (c) represent adjacent flight lines with a 6 ~~minutes~~min time gap. These flight lines can be
divided into three regions: region A covers no NO₂ source but is affected by the carbon factories ~~about~~approximately 3 km
away; region B covers the steel factory as the dominant NO₂ source; region C covers no NO₂ source and is not affected by
other sources. ~~Compared to region B, there is a large temporal variety of NO₂ VCDs in region A between three flight lines.
Region C is temporally consistent with relatively low NO₂ columns. From these observations it may be concluded that
largest temporal variability could occur where there is no local NO₂ source but is down wind of other sources, especially
when wind direction is changing.~~In these three regions, only region C is temporally consistent with relatively low NO₂
595 columns, whilst a large temporal variety of NO₂ VCDs exists in region A and region B because of inconstant emission
sources and changing meteorology.

600 6 NO₂ VCD assessment

6.1 Uncertainty analysis

The total uncertainty on the retrieved tropospheric NO₂ VCDs is composed of three parts: (1) uncertainties in the retrieved
dSCDs; ~~;~~ (2) uncertainties in reference column SCD_{ref}; ~~;~~ and (3) uncertainties in computed AMFs. Assuming that these
uncertainties originating from independent steps are sufficiently uncorrelated, the total uncertainty of the tropospheric NO₂
605 VCD can be quantified as follows:

$$\sigma_{\text{VCD}_i} = \sqrt{\left(\frac{\sigma_{\text{dSCD}_i}}{\text{AMF}_i}\right)^2 + \left(\frac{\sigma_{\text{SCD}_{\text{ref}}}}{\text{AMF}_i}\right)^2 + \left(\frac{\text{SCD}_i}{\text{AMF}_i^2} \times \sigma_{\text{AMF}_i}\right)^2}. \quad (2)$$

The first uncertainty source, σ_{dSCD_i} , originates from the DOAS fit residuals and is a direct output in the QDOAS software. This dSCD uncertainty is dominated by the shot noise from radiance, the electronic noise from the instrument, the systematic uncertainties from the cross sections and the errors from wavelength calibration. In this study, spatial binning of 10 pixels is performed to reduce ~~this-these~~ DOAS fit residuals, with a mean slant error of 4.8×10^{15} molec cm^{-2} . ~~Compared to mobile DOAS system, this DOAS fit error is approximately two times larger. Unlikely situation of mobile DOAS system, it becomes a major contributor to the total uncertainty in the case of an airborne sensor, especially in a clean area.~~

The second uncertainty source, $\sigma_{\text{SCD}_{\text{ref}}}$, is caused by the NO_2 residual amount in the reference spectra. Since we use the TROPOMI tropospheric NO_2 product of the clean reference area as the background amount, the uncertainty of NO_2 vertical column is estimated to be 1×10^{15} molec cm^{-2} directly from TROPOMI product. ~~Assuming a~~ tropospheric AMF of 2.0 and a tropospheric AMF over the reference spectra of 1.8, ~~this results result in~~ an uncertainty 9×10^{14} molec cm^{-2} to the tropospheric vertical column.

The third uncertainty source, σ_{AMF_i} , derives from the uncertainties in the parameter assumptions of radiative transfer model inputs. According to previous studies (Boersma et al., 2004; Pope et al., 2015), ~~it- σ_{AMF_i}~~ is treated as systematic and depends on the surface albedo, the NO_2 profile, the aerosol parameters, and the cloud fraction. (1) ~~Since the research flight took place under cloudless conditions, cloud fraction is neglected in this case. The cloud fraction is neglected in this case because the research flight was under cloudless conditions.~~ (2) ~~Results-The results~~ of the dependence tests in Seet-Section 4.3.2 suggest that the surface albedo has the most significant effect on the AMF. According to Vermote et al. (2016), the uncertainty of the LANDSAT 8 surface reflectance product of band 1 is 0.011. (3) ~~Based on~~ According to the sensitivity study performed in Seet-Section 4.3.2, the uncertainty related to the a priori NO_2 profile shape is lower than 22 %. (4) According to the performed simulations of a pure Rayleigh atmosphere, the uncertainty related to the aerosol state is estimated to be less than 1 %. (5) Because of the high accuracy of the viewing and sun ~~geometry, geometries~~ and ~~its-their~~ low impact on the AMF computation revealed in the previous section, the uncertainty related to the viewing and sun ~~geometry-geometries~~ is expected to be ~~ignorable-negligible~~. Therefore, combining all the uncertainty sources in the quadrature, a mean relative uncertainty of 24 % on the σ_{AMF_i} is obtained.

Based on above discussion, the total uncertainties on the retrieved tropospheric NO_2 VCDs of all the observations of the research flight are calculated. ~~They,~~ typically ~~range between~~ ranging from 4.5 and 1.5×10^{15} to 5.9×10^{15} molec cm^{-2} , with a mean value of 3.0×10^{15} molec cm^{-2} .

6.2 Comparison to mobile DOAS measurements

In order to compare the UVHIS NO_2 VCDs to the ground-based measurements, mobile DOAS observations were performed on 23 June 2018 ~~as well~~. This mobile DOAS system is composed of a spectrum acquisition unit and a GPS module. The spectrum collection unit consists of a spectrometer, a telescope, an optical ~~fiber-fibre~~, and a workbench. The FOV of this telescope is 0.3° , and its focal length is 69 mm. The spectrometer used is a Maya 2000 Pro spectrometer, with a wavelength

range of 290–420 nm and a spectral resolution of 0.55 nm. ~~Zenith-sky~~The zenith-sky observations of the mobile DOAS ~~are~~
640 ~~were~~ adopted for minimal blocking of buildings and trees in this research. The important properties of the mobile DOAS
system and its NO₂ retrieval approach are shown in Table 5. It is worth noting that the retrieval window in the mobile DOAS
observations differs from the one used for the airborne observations.

For better comparison with the UVHIS NO₂ observations, assumptions and parameters in the tropospheric NO₂ retrieval
method for the mobile DOAS were similarly set to ~~the same as those of~~ the UVHIS. For example, the residual amount of NO₂
645 in the reference spectra was set to 3×10^{15} molec cm⁻² with an error of 1×10^{15} molec cm⁻²; the mobile DOAS observations
only focused on the tropospheric portion of the NO₂ columns, ~~assumed~~assuming that the difference ~~of in~~ the stratospheric
NO₂ columns between the observed ~~spectra~~ and reference spectra is negligible; the vertical profiles of NO₂ and aerosol
extinction, albedo, and aerosol properties in the AMF calculation were similarly set to ~~the same as those of the~~ UVHIS.

Like the uncertainty analysis of the UVHIS NO₂ columns, the total uncertainty on the retrieved mobile tropospheric VCD is
650 composed of three parts: (1) the mean uncertainty on the dSCD of the mobile DOAS is 1.4×10^{15} molec cm⁻²; (2) the
uncertainty of reference vertical column is estimated to be 1×10^{15} molec cm⁻². In the case that the tropospheric AMFs of
the measured and reference spectra are very close, this part results in an uncertainty of 1×10^{15} molec cm⁻² to the total
uncertainty; (3) the mean relative uncertainty on the AMF calculation is 22 % by the square root of the quadratic sum of the
individual uncertainties like UVHIS. Combining these uncertainties together, the mean total uncertainties on the retrieved
655 tropospheric NO₂ VCD is 2.1×10^{15} molec cm⁻².

Basically, the route of the mobile DOAS was designed to encircle the power plant and the steel factory which are supposed
to be predominant sources. For ~~the~~ comparison, the mobile DOAS observations are first gridded to the same sampling of the
UVHIS pixels, ~~then~~Then the VCD of the UVHIS NO₂ results is extracted for each co-located mobile measurement. An
overview of the mobile DOAS measurements over the UVHIS NO₂ layer is shown in Fig. 13. The NO₂ distributions of the
660 mobile DOAS system and the UVHIS exhibit similar spatial characteristics, which i.e. low values are ~~located~~ in the south of
the steel factory and power plant, and high values are inside the plumes.

Figure 14 (a) shows scatter plots with the VCDs retrieved by the UVHIS on the x-axis and the mobile DOAS VCDs on the
y-axis, for all co-located measurements. The corresponding results of the linear regression analysis are also provided in
Fig.14 (a), with a correlation coefficient of 0.69, a slope of 1.30, and an intercept of -9.01×10^{14} . The absolute time offset
665 between the mobile DOAS and airborne observations can be up to 1 ~~hourh~~, which means indicating that both instruments
cannot sample the NO₂ column at certain geolocations simultaneously. As shown in Fig. 14 (b), when only comparing
UVHIS VCDs to mobile measurements that circled the steel factory, the correlation coefficient ~~improves~~improved to 0.86.
In this case, all mobile measurements occurred inside the swath of one flight line of aircraft, and the time offset between two
instruments shortened to 15 ~~minutes~~min. In general, an underestimation of the UVHIS VCDs of increased value can be
670 observed in Figs 14 (a) and (b). Considering the variability in local emissions and meteorology, it is reasonable that the

differences between these two instruments exist. ~~Besides, the averaging effect of the area inside an UVHIS pixel can also lead to the underestimation of UVHIS compared to mobile DOAS system.~~ A sensitivity test of the AMF on the NO₂ profile was performed for all co-located measurements, using a box profile of 500 m. Compared to the box profile of 2 km, the UVHIS AMFs decreased by an average of 17 %, whilst the mobile DOAS AMFs decreased by an average of 2.7 %. This results suggest that a more realistic profile with the NO₂ layer closer to the ground could improve the slope closer to unity.

7 Conclusions

In this paper, we present the newly developed ~~Ultraviolet Visible Hyperspectral Imaging Spectrometer (UVHIS)~~ UVHIS instrument, with a broad spectral region ranging from 200 to 500 nm, and a high spectral resolution better than 0.5 nm. The instrument is operated in three channels at wavelength 200 to 276 nm (channel 1), 276 to 380 nm (channel 2), and 380 to 500 nm (channel 3) for minimal stray light effects and the highest spectral performance. The optical design of each channel consists of a fore-optics with a FOV of 40°, an Offner imaging spectrometer, and a CCD array detector of 1032 × 1072 pixels.

~~Also we~~ We also present the first tropospheric NO₂ retrieval results from the UVHIS airborne observation in June 2018. The research flight ~~above-over~~ Feicheng, China, covered an area of ~~approximately about 20-30 × 30-20~~ km² within 3 ~~hourh~~, with a high spatial resolution ~~about approximately~~ 25 × 22 m². We first retrieved d the differential NO₂ slant column densities from nadir observed spectra by ~~application of applying the~~ DOAS technique, to a mean reference spectra over a clean area. Then we converted d those NO₂ slant columns to tropospheric vertical columns using the air mass factors derived from the SCIATRAN model with the Landsat 8 surface reflectance product. ~~Total-The total~~ uncertainties of the tropospheric NO₂ vertical columns ~~are in range of range from~~ 1.5×10^{15} to 5.9×10^{15} molec cm⁻², with a mean value of 3.0×10^{15} molec cm⁻².

The two-dimensional distribution map of the tropospheric NO₂ VCD demonstrates that the UVHIS is adequate for trace gas pollution monitoring over a large area in a relatively short time frame. With the high spatial resolution of the UVHIS, different local emission sources can be distinguished, fine-scale horizontal variability can be revealed, and trace gas emission and transmission can be understood. For the flight on 23 June 2018, the NO₂ distribution ~~is-was~~ dominated by several exhaust plumes which exhibited the same south to north direction of transmission, with a peak value of 3×10^{16} molec cm⁻² in the dominant plume. ~~Comparisons-The comparisons~~ of the UVHIS NO₂ vertical columns ~~to-with the~~ mobile DOAS observations show a good overall agreement-overall, with a correlation coefficient of 0.65 for all the co-located measurements, and a correlation coefficient of 0.86 for the co-located measurements that only circled the steel factory. However, an underestimation of the high NO₂ columns of the UVHIS is observed relative to the mobile DOAS measurements.

~~High-resolution~~ The high-resolution information about the NO₂ horizontal distribution, generated from UVHIS airborne data, is unique and valuable compared to those from ground-based instruments and space-borne sensors. In future study, the

UVHIS could be applied in the validation of satellite trace gas instruments, and in the connection between local point observations, air quality models, and global monitoring from space.

705 *Data availability.* The datasets in the present work are available from the corresponding author upon reasonable request.

Author Contributions. ConceptualizationConceptualisation, F.S.; methodology, Y.J. and H.Z.; software, Z.C.; validation, X.Q. and D.Y.; formal analysis, L.X.; resources, K.Z.; writing—original draft preparation, L.X.; writing—review and editing, F.S.

710 *Competing Interest.* The authors declare no conflict of interest.

Acknowledgments. We would like to thank Thomas Danckaert, Caroline Fayt and Michel Van Roozendaal for help on QDOAS software. We are thankful to the following agencies for providing the satellite data: The Sentinel 5 Precursor TROPOMI Level 2 NO₂ product is developed by KNMI with funding from the Netherlands Space Office (NSO) and processed with funding from the European Space Agency (ESA). TROPOMI data can be downloaded from <https://s5phub.copernicus.eu>. Landsat 8 OLI data have been produced, archived, and distributed by the U.S. Geological Survey (USGS). The original Landsat surface reflectance algorithm was developed by Dr. Eric Vermote, NASA Goddard Space Flight Center (GSFC). Landsat 8 OLI data are available at <https://earthexplorer.usgs.gov>.

720 *Financial support.* This research was supported by grants from the National Key Research and Development Program of China (Nos. 2016YFC0200402, 2019YFC0214702).

References

- An, Z., Huang, R.-J., Zhang, R., Tie, X., Li, G., Cao, J., Zhou, W., Shi, Z., Han, Y., Gu, Z. and Ji, Y.: Severe haze in northern China: A synergy of anthropogenic emissions and atmospheric processes, *Proc. Natl. Acad. Sci.*, 116(18), 8657–8666, doi:10.1073/pnas.1900125116, 2019.
- 725 Barsi, J., Schott, J., Hook, S., Raqueno, N., Markham, B. and Radocinski, R.: Landsat-8 Thermal Infrared Sensor (TIRS) Vicarious Radiometric Calibration, *Remote Sens.*, 6(11), 11607–11626, doi:10.3390/rs61111607, 2014.
- Boersma, K. F., Eskes, H. J. and Brinksma, E. J.: Error analysis for tropospheric NO₂ retrieval from space, *J. Geophys. Res. Atmospheres*, 109(D4), doi:10.1029/2003JD003962, 2004.
- 730 Bovensmann, H., Burrows, J. P., Buchwitz, M. and Frerick, J.: SCIAMACHY: Mission Objectives and Measurement Modes, *J. ATMOSPHERIC Sci.*, 56, 24, 1999.
- Burrows, J. P., Weber, M., Buchwitz, M., Rozanov, V., TTER-WEIßENMAYER, A. L., Richter, A., Bramstedt, K., Eichmann, K.-U., Eisinger, M. and Perner, D.: The Global Ozone Monitoring Experiment (GOME): Mission Concept and First Scientific Results, *J. ATMOSPHERIC Sci.*, 56, 25, 1999.

- 735 Chance, K. and Kurucz, R. L.: An improved high-resolution solar reference spectrum for earth's atmosphere measurements in the ultraviolet, visible, and near infrared, *J. Quant. Spectrosc. Radiat. Transf.*, 111(9), 1289–1295, doi:10.1016/j.jqsrt.2010.01.036, 2010.
- Chance, K. V. and Spurr, R. J. D.: Ring effect studies: Rayleigh scattering, including molecular parameters for rotational Raman scattering, and the Fraunhofer spectrum, *Appl. Opt.*, 36(21), 5224, doi:10.1364/AO.36.005224, 1997.
- 740 Cheng, L., Tao, J., Valks, P., Yu, C., Liu, S., Wang, Y., Xiong, X., Wang, Z. and Chen, L.: NO₂ Retrieval from the Environmental Trace Gases Monitoring Instrument (EMI): Preliminary Results and Intercomparison with OMI and TROPOMI, *Remote Sens.*, 11(24), 3017, doi:10.3390/rs11243017, 2019.
- Crippa, M., Guizzardi, D., Muntean, M., Schaaf, E., Dentener, F., van Aardenne, J. A., Monni, S., Doering, U., Olivier, J. G. J., Pagliari, V. and Janssens-Maenhout, G.: Gridded Emissions of Air Pollutants for the period 1970–2012 within EDGAR v4.3.2, preprint, Data, Algorithms, and Models., 2018.
- 745 Danckaert, T., Fayt, C., Roozendaal, M. V., Smedt, I. D., Letocart, V., Merlaud, A. and Pinardi, G.: QDOAS Software user manual, [online] Available from: http://uv-vis.aeronomie.be/software/QDOAS/QDOAS_manual.pdf (Accessed 2 June 2020), 2020.
- 750 General, S., Pöhler, D., Sihler, H., Bobrowski, N., Frieß, U., Zielcke, J., Horbanski, M., Shepson, P. B., Stirm, B. H., Simpson, W. R., Weber, K., Fischer, C. and Platt, U.: The Heidelberg Airborne Imaging DOAS Instrument (HAIDI) – a novel imaging DOAS device for 2-D and 3-D imaging of trace gases and aerosols, *Atmospheric Meas. Tech.*, 7(10), 3459–3485, doi:10.5194/amt-7-3459-2014, 2014.
- Heue, K.-P., Wagner, T., Broccardo, S. P., Walter, D., Piketh, S. J., Ross, K. E., Beirle, S. and Platt, U.: Direct observation of two dimensional trace gas distributions with an airborne Imaging DOAS instrument, *Atmospheric Chem. Phys.*, 8(22), 6707–6717, doi:10.5194/acp-8-6707-2008, 2008.
- 755 Lamsal, L. N., Janz, S. J., Krotkov, N. A., Pickering, K. E., Spurr, R. J. D., Kowalewski, M. G., Loughner, C. P., Crawford, J. H., Swartz, W. H. and Herman, J. R.: High-resolution NO₂ observations from the Airborne Compact Atmospheric Mapper: Retrieval and validation, *J. Geophys. Res. Atmospheres*, 122(3), 1953–1970, doi:10.1002/2016JD025483, 2017.
- 760 Lawrence, J. P., Anand, J. S., Vande Hey, J. D., White, J., Leigh, R. R., Monks, P. S. and Leigh, R. J.: High-resolution measurements from the airborne Atmospheric Nitrogen Dioxide Imager (ANDI), *Atmospheric Meas. Tech.*, 8(11), 4735–4754, doi:10.5194/amt-8-4735-2015, 2015.
- Levelt, P. F., van den Oord, G. H. J., Dobber, M. R., Malkki, A., Huib Visser, Johan de Vries, Stammes, P., Lundell, J. O. V. and Saari, H.: The ozone monitoring instrument, *IEEE Trans. Geosci. Remote Sens.*, 44(5), 1093–1101, doi:10.1109/TGRS.2006.872333, 2006.
- 765 Li, Z. Q., Xu, H., Li, K. T., Li, D. H., Xie, Y. S., Li, L., Zhang, Y., Gu, X. F., Zhao, W., Tian, Q. J., Deng, R. R., Su, X. L., Huang, B., Qiao, Y. L., Cui, W. Y., Hu, Y., Gong, C. L., Wang, Y. Q., Wang, X. F., Wang, J. P., Du, W. B., Pan, Z. Q., Li, Z. Z. and Bu, D.: Comprehensive Study of Optical, Physical, Chemical, and Radiative Properties of Total Columnar Atmospheric Aerosols over China: An Overview of Sun–Sky Radiometer Observation Network (SONET) Measurements, *Bull. Am. Meteorol. Soc.*, 99(4), 739–755, doi:10.1175/BAMS-D-17-0133.1, 2018.
- 770 Liu, F., Beirle, S., Zhang, Q., van der A, R. J., Zheng, B., Tong, D. and He, K.: NO_x emission trends over Chinese cities estimated from OMI observations during 2005 to 2015, *Atmospheric Chem. Phys.*, 17(15), 9261–9275, doi:10.5194/acp-17-9261-2017, 2017.

- Liu, J., Si, F., Zhou, H., Zhao, M., Dou, K., Wang, Y. and Liu, W.: Observation of two-dimensional distributions of NO₂ with airborne imaging DOAS technology, *Acta Phys. Sin.*, 64(3), 034217, doi:10.7498/aps.64.034217, 2015.
- 775 Meier, A. C., Schönhardt, A., Bösch, T., Richter, A., Seyler, A., Ruutz, T., Constantin, D.-E., Shaiganfar, R., Wagner, T., Merlaud, A., Van Roozendaal, M., Belegante, L., Nicolae, D., Georgescu, L. and Burrows, J. P.: High-resolution airborne imaging DOAS measurements of NO₂ above Bucharest during AROMAT, *Atmospheric Meas. Tech.*, 10(5), 1831–1857, doi:10.5194/amt-10-1831-2017, 2017.
- 780 Munro, R., Lang, R., Klaes, D., Poli, G., Retscher, C., Lindstrot, R., Huckle, R., Lacan, A., Grzegorski, M., Holdak, A., Kokhanovsky, A., Livschitz, J. and Eisinger, M.: The GOME-2 instrument on the Metop series of satellites: instrument design, calibration, and level 1 data processing – an overview, *Atmospheric Meas. Tech.*, 9(3), 1279–1301, doi:10.5194/amt-9-1279-2016, 2016.
- 785 Nowlan, C. R., Liu, X., Leitch, J. W., Chance, K., González Abad, G., Liu, C., Zoogman, P., Cole, J., Delker, T., Good, W., Murcray, F., Ruppert, L., Soo, D., Follette-Cook, M. B., Janz, S. J., Kowalewski, M. G., Loughner, C. P., Pickering, K. E., Herman, J. R., Beaver, M. R., Long, R. W., Szykman, J. J., Judd, L. M., Kelley, P., Luke, W. T., Ren, X. and Al-Saadi, J. A.: Nitrogen dioxide observations from the Geostationary Trace gas and Aerosol Sensor Optimization (GeoTASO) airborne instrument: Retrieval algorithm and measurements during DISCOVER-AQ Texas 2013, *Atmospheric Meas. Tech.*, 9(6), 2647–2668, doi:10.5194/amt-9-2647-2016, 2016.
- Platt, U. and Stutz, J.: *Differential Optical Absorption Spectroscopy: Principles and Applications*, Springer-Verlag, Berlin, Germany., 2008.
- 790 Pope, R. J., Chipperfield, M. P., Savage, N. H., Ordóñez, C., Neal, L. S., Lee, L. A., Dhomse, S. S., Richards, N. A. D. and Keslake, T. D.: Evaluation of a regional air quality model using satellite column NO₂ treatment of observation errors and model boundary conditions and emissions, *Atmospheric Chem. Phys.*, 15(10), 5611–5626, doi:10.5194/acp-15-5611-2015, 2015.
- 795 Popp, C., Brunner, D., Damm, A., Van Roozendaal, M., Fayt, C. and Buchmann, B.: High-resolution NO₂ remote sensing from the Airborne Prism EXperiment (APEX) imaging spectrometer, *Atmospheric Meas. Tech.*, 5(9), 2211–2225, doi:10.5194/amt-5-2211-2012, 2012.
- QGIS development team: QGIS Geographic Information System, Open Source Geospatial Foundation, QGIS Geogr. Inf. Syst. Open Source Geospatial Found. [online] Available from: <https://www.qgis.org/en/site/> (Accessed 2 June 2020), 2020.
- 800 Remer, L. A., Kaufman, Y. J., Tanré, D., Mattoo, S., Chu, D. A., Martins, J. V., Li, R.-R., Ichoku, C., Levy, R. C., Kleidman, R. G., Eck, T. F., Vermote, E. and Holben, B. N.: The MODIS Aerosol Algorithm, Products, and Validation, *J. Atmospheric Sci.*, 62(4), 947–973, doi:10.1175/JAS3385.1, 2005.
- 805 Rothman, L. S., Gordon, I. E., Babikov, Y., Barbe, A., Chris Benner, D., Bernath, P. F., Birk, M., Bizzocchi, L., Boudon, V., Brown, L. R., Campargue, A., Chance, K., Cohen, E. A., Coudert, L. H., Devi, V. M., Drouin, B. J., Fayt, A., Flaud, J.-M., Gamache, R. R., Harrison, J. J., Hartmann, J.-M., Hill, C., Hodges, J. T., Jacquemart, D., Jolly, A., Lamouroux, J., Le Roy, R. J., Li, G., Long, D. A., Lyulin, O. M., Mackie, C. J., Massie, S. T., Mikhailenko, S., Müller, H. S. P., Naumenko, O. V., Nikitin, A. V., Orphal, J., Perevalov, V., Perrin, A., Polovtseva, E. R., Richard, C., Smith, M. A. H., Starikova, E., Sung, K., Tashkun, S., Tennyson, J., Toon, G. C., Tyuterev, V. G. and Wagner, G.: The HITRAN2012 molecular spectroscopic database, *J. Quant. Spectrosc. Radiat. Transf.*, 130, 4–50, doi:10.1016/j.jqsrt.2013.07.002, 2013.
- 810 Rozanov, V. V., Rozanov, A. V., Kokhanovsky, A. A. and Burrows, J. P.: Radiative transfer through terrestrial atmosphere and ocean: Software package SCIATRAN, *J. Quant. Spectrosc. Radiat. Transf.*, 133, 13–71, doi:10.1016/j.jqsrt.2013.07.004, 2014.

- Schönhardt, A., Altube, P., Gerilowski, K., Krautwurst, S., Hartmann, J., Meier, A. C., Richter, A. and Burrows, J. P.: A wide field-of-view imaging DOAS instrument for two-dimensional trace gas mapping from aircraft, *Atmospheric Meas. Tech.*, 8(12), 5113–5131, doi:10.5194/amt-8-5113-2015, 2015.
- 815 Seinfeld, J. H. and Pandis, S. N.: *Atmospheric chemistry and physics: from air pollution to climate change*, Third edition., John Wiley & Sons, Hoboken, New Jersey., 2016.
- Serdyuchenko, A., Gorshchev, V., Weber, M., Chehade, W. and Burrows, J. P.: High spectral resolution ozone absorption cross-sections - Part 2: Temperature dependence, *Atmospheric Meas. Tech.*, 7(2), 625–636, doi:10.5194/amt-7-625-2014, 2014.
- 820 Solomon, S.: Stratospheric ozone depletion: A review of concepts and history, *Rev. Geophys.*, 37(3), 275–316, doi:10.1029/1999RG900008, 1999.
- Solomon, S., Schmeltekopf, A. L. and Sanders, R. W.: On the interpretation of zenith sky absorption measurements, *J. Geophys. Res.*, 92(D7), 8311, doi:10.1029/JD092iD07p08311, 1987.
- 825 Tack, F., Merlaud, A., Iordache, M.-D., Danckaert, T., Yu, H., Fayt, C., Meuleman, K., Deutsch, F., Fierens, F. and Van Roozendael, M.: High-resolution mapping of the NO₂ spatial distribution over Belgian urban areas based on airborne APEX remote sensing, *Atmospheric Meas. Tech.*, 10(5), 1665–1688, doi:10.5194/amt-10-1665-2017, 2017.
- Tack, F., Merlaud, A., Meier, A. C., Vlemmix, T., Ruhtz, T., Iordache, M.-D., Ge, X., van der Wal, L., Schuettmeyer, D., Ardelean, M., Calcan, A., Constantin, D., Schönhardt, A., Meuleman, K., Richter, A. and Van Roozendael, M.: Intercomparison of four airborne imaging DOAS systems for tropospheric NO₂ mapping – the AROMAPEX campaign, *Atmospheric Meas. Tech.*, 12(1), 211–236, doi:10.5194/amt-12-211-2019, 2019.
- 830 Thalman, R. and Volkamer, R.: Temperature dependent absorption cross-sections of O₂–O₂ collision pairs between 340 and 630 nm and at atmospherically relevant pressure, *Phys. Chem. Chem. Phys.*, 15(37), 15371, doi:10.1039/c3cp50968k, 2013.
- Vandaele, A. C., Hermans, C., Simon, P. C., Carleer, M., Colin, R., Fally, S., Mérienne, M. F., Jenouvrier, A. and Coquart, B.: Measurements of the NO₂ absorption cross-section from 42 000 cm⁻¹ to 10 000 cm⁻¹ (238–1000 nm) at 220 K and 294 K, *J. Quant. Spectrosc. Radiat. Transf.*, 59(3–5), 171–184, doi:10.1016/S0022-4073(97)00168-4, 1998.
- 835 Veeffkind, J. P., Aben, I., McMullan, K., Förster, H., de Vries, J., Otter, G., Claas, J., Eskes, H. J., de Haan, J. F., Kleipool, Q., van Weele, M., Hasekamp, O., Hoogeveen, R., Landgraf, J., Snel, R., Tol, P., Ingmann, P., Voors, R., Kruizinga, B., Vink, R., Visser, H. and Levelt, P. F.: TROPOMI on the ESA Sentinel-5 Precursor: A GMES mission for global observations of the atmospheric composition for climate, air quality and ozone layer applications, *Remote Sens. Environ.*, 120, 70–83, doi:10.1016/j.rse.2011.09.027, 2012.
- Vermote, E., Justice, C., Claverie, M. and Franch, B.: Preliminary analysis of the performance of the Landsat 8/OLI land surface reflectance product, *Remote Sens. Environ.*, 11, 2016.
- Vermote, E. F., Tanre, D., Deuze, J. L., Herman, M. and Morcette, J.-J.: Second Simulation of the Satellite Signal in the Solar Spectrum, 6S: an overview, *IEEE Trans. Geosci. Remote Sens.*, 35(3), 675–686, doi:10.1109/36.581987, 1997.
- 845 Zhang, C., Liu, C., Hu, Q., Cai, Z., Su, W., Xia, C., Zhu, Y., Wang, S. and Liu, J.: Satellite UV-Vis spectroscopy: implications for air quality trends and their driving forces in China during 2005–2017, *Light Sci. Appl.*, 8(1), 100, doi:10.1038/s41377-019-0210-6, 2019.

850 Zhang, C., Liu, C., Chan, K. L., Hu, Q., Liu, H., Li, B., Xing, C., Tan, W., Zhou, H., Si, F. and Liu, J.: First observation of tropospheric nitrogen dioxide from the Environmental Trace Gases Monitoring Instrument onboard the GaoFen-5 satellite, *Light Sci. Appl.*, 9(1), 66, doi:10.1038/s41377-020-0306-z, 2020.

Zhang, Q., Huang, S., Zhao, X., Si, F., Zhou, H., Wang, Y. and Liu, W.: The Design and Implementation of CCD Refrigeration System of Imaging Spectrometer, *Acta Photonica Sin.*, 46(3), 0311004, 2017.

855 Zhao, M. J., Si, F. Q., Zhou, H. J., Wang, S. M., Jiang, Y. and Liu, W. Q.: Preflight calibration of the Chinese Environmental Trace Gases Monitoring Instrument (EMI), *Atmospheric Meas. Tech.*, 11(9), 5403–5419, doi:10.5194/amt-11-5403-2018, 2018.

860

865

870

875

880

Table 1: UVHIS instrument characteristics of three channels.

Characteristic	Channel 1	Channel 2	Channel 3
Wavelength range	200–276 nm	276–380 nm	380–500 nm
Spectral sampling	0.074 nm	0.10 nm	0.12 nm
Spectral resolution	0.34 nm	0.46 nm	0.49 nm
FOV	40°	40°	40°
Focal length	18 mm	18 mm	18 mm
Across-track angular resolution	0.5 mrad	0.5 mrad	0.5 mrad
f-number	3.4	3.6	3.6
Detector size	1032 × 1072	1032 × 1072	1032 × 1072

885

Table 2. Preflight wavelength calibration results (FWHMs) of UVHIS channel 3 for 9 viewing angles. Light sources used in the calibration are a mercury-argon lamp and a [tunable laser](#). Slit function shapes are retrieved by least square fitting of characteristic spectral lines, using a symmetric Gaussian function.

890

FOV	379.887 nm	404.656 nm	450.504 nm	500.566 nm
-20°	0.35 nm	0.35 nm	0.39 nm	0.50 nm
-15°	0.33 nm	0.31 nm	0.33 nm	0.43 nm
-10°	0.31 nm	0.29 nm	0.29 nm	0.41 nm
-5°	0.31 nm	0.30 nm	0.29 nm	0.34 nm
0°	0.31 nm	0.32 nm	0.30 nm	0.30 nm
5°	0.34 nm	0.36 nm	0.34 nm	0.30 nm
10°	0.38 nm	0.39 nm	0.38 nm	0.32 nm
15°	0.40 nm	0.44 nm	0.42 nm	0.35 nm
20°	0.45 nm	0.46 nm	0.47 nm	0.38 nm

895

Table 3. Main analysis parameters and absorption cross sections for NO₂ DOAS retrieval.

Parameter	Settings
Wavelength calibration	Solar atlas, (Chance and Kurucz, 2010)
Fitting interval	430–470 nm
Cross sections	
NO ₂	298 K, Vandaele et al. (1998)
O ₃	223 K, Serdyuchenko et al. (2014)
O ₄	293 K, Thalman and Volkamer (2013)
H ₂ O	293 K, Rothman et al. (2013)
Ring effect	Chance and Spurr (1997)
Polynomial term	Order 5
Intensity offset <u>Offset</u>	Order 1

900

905

Table 4. Overview of the input parameters in the SCIATRAN RTM, characterizing the AMF LUT.

RTM Parameter	Grid settings
Wavelength	450 nm
Sensor altitude	3 km
Surface reflectance	0.01–0.4 (steps of 0.01)
Solar zenith angle	10–40° (steps of 10°)
Viewing zenith angle	0–40° (steps of 10°)
Relative azimuth angle	0–180° (steps of 30°)
Aerosol optical depth	0–1 (steps of 0.1)
Aerosol extinction profile	Box of 2.0 km
NO ₂ profile	Box of 2.0 km

910

Table 5. Properties of the mobile DOAS system and its NO₂ fit.

Parameter	Settings
Elevation angle	zenith
Fitting interval	356–376 nm
Wavelength calibration	Mercury lamp
Cross sections	
NO ₂	298 K, Vandaele et al. (1998)
O ₃	223 K, Serdyuchenko et al. (2014)
O ₄	293 K, Thalman and Volkamer (2013)
Ring effect	Chance and Spurr (1997)
Polynomial term	Order 5
Intensity offset <u>Offset</u>	Order 1

915

920

925

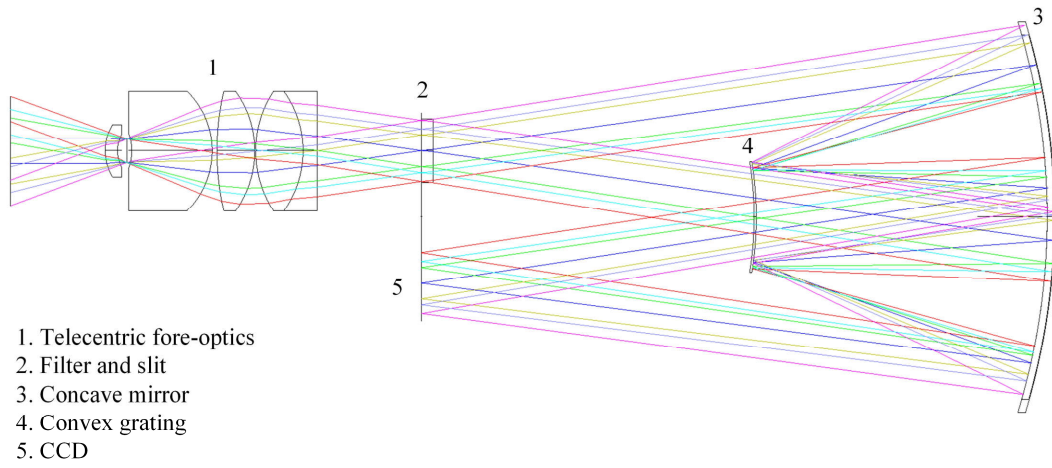


Figure 1. Optical layout of the UVHIS channel 3. Optical design of channel 1 and channel 2 is similar.

930

935

940

945

950

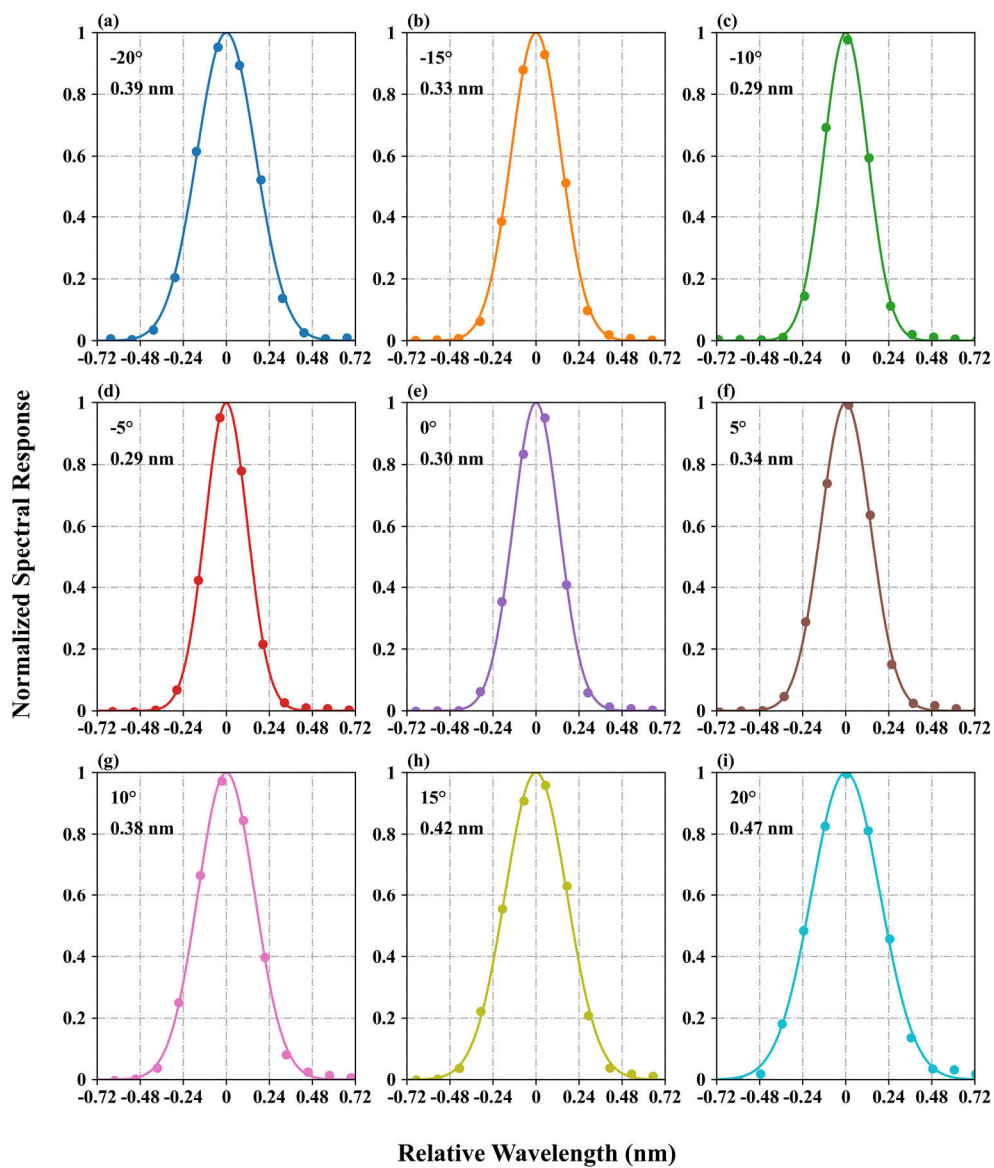
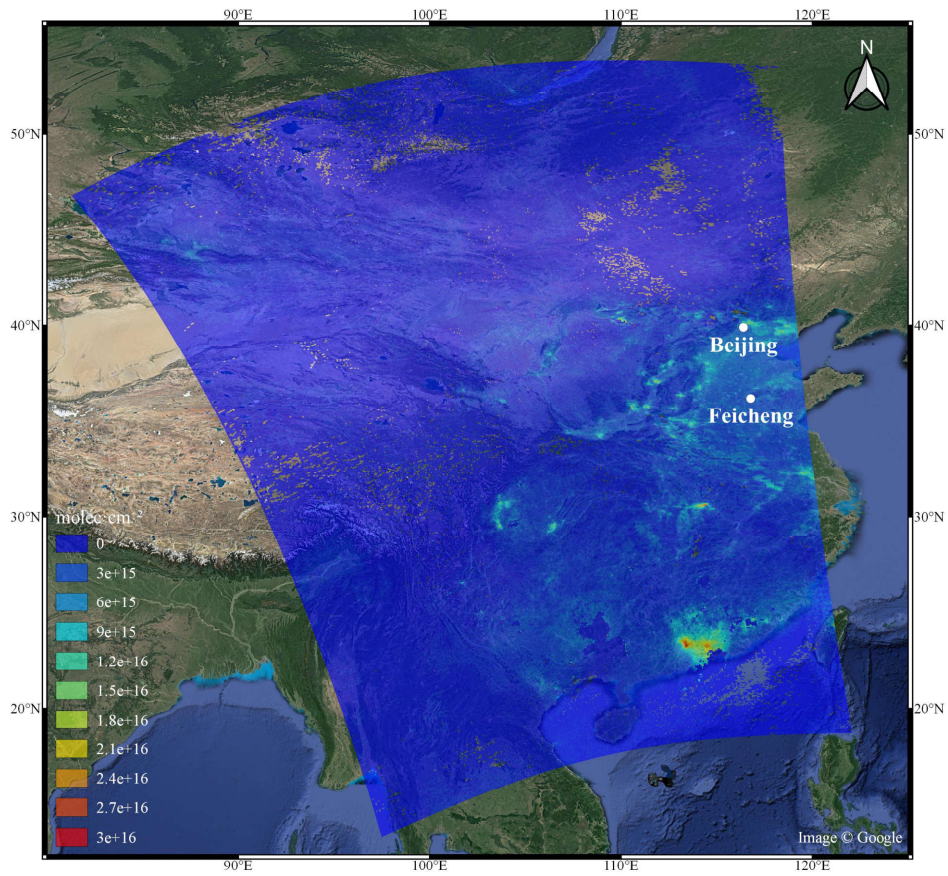
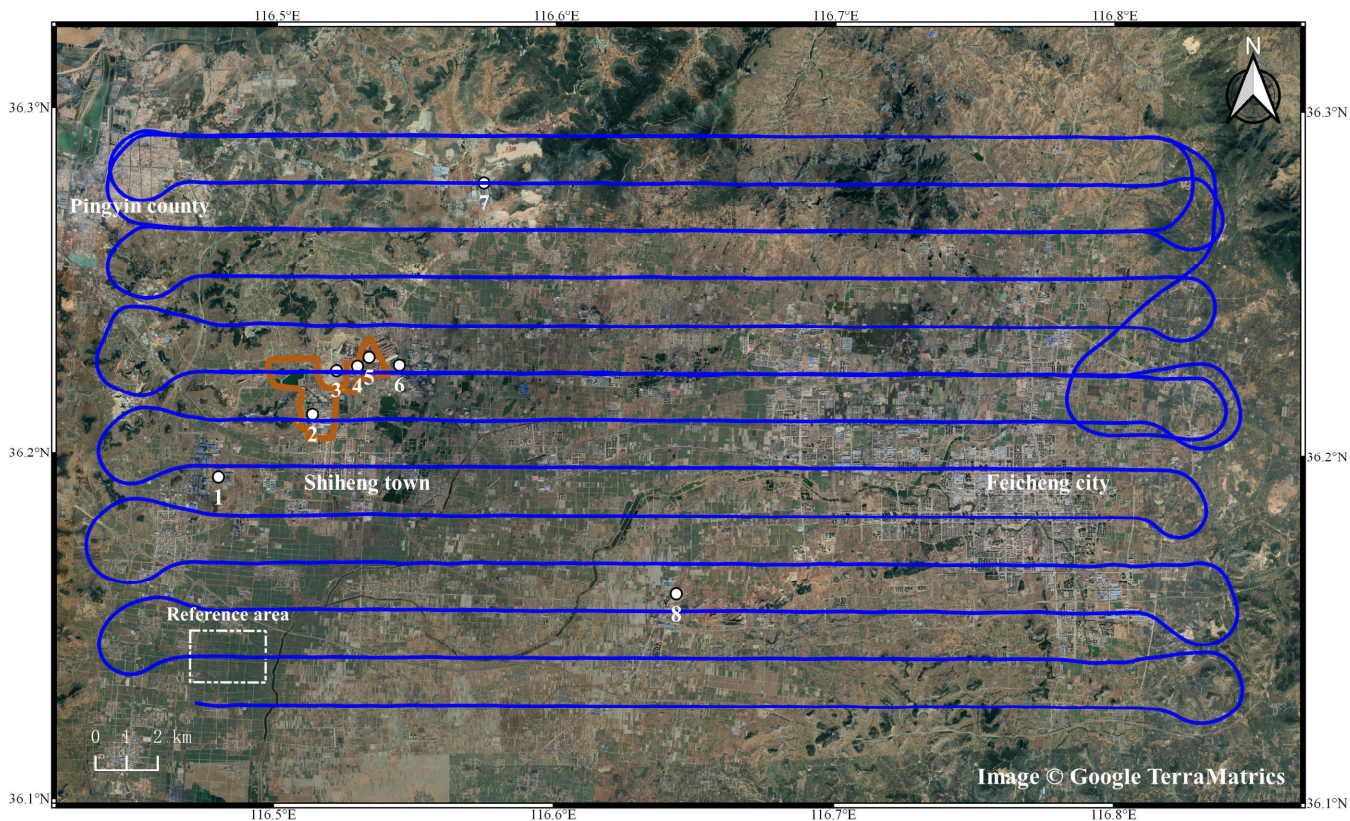


Figure 2. Measured slit functions (dots) at 450.504 nm and retrieved slit function shapes (lines) using a symmetric Gaussian function for 9 viewing angles.



955

Figure 3. TROPOMI observation of tropospheric NO₂ over China on 23 June, 2018. The location of UVHIS flight (Feicheng city) is also plotted in the map.



960 **Figure 4.** Overview of the Feicheng demonstration flight on 23 June, 2018. Flight lines are shown in blue. Two orange circles represent
 965 the routes of mobile DOAS system. White dots numbered from 1 to 8 represent the major emission sources. Number 1: several carbon
 factories; number 2: a power plant; numbers 3-6: individual emitters inside the steel factories, while numbers 4 and 5 are inside the circle
 of one mobile DOAS route; numbers 7-8: two cement factories. White dashed box represents the reference area.

965

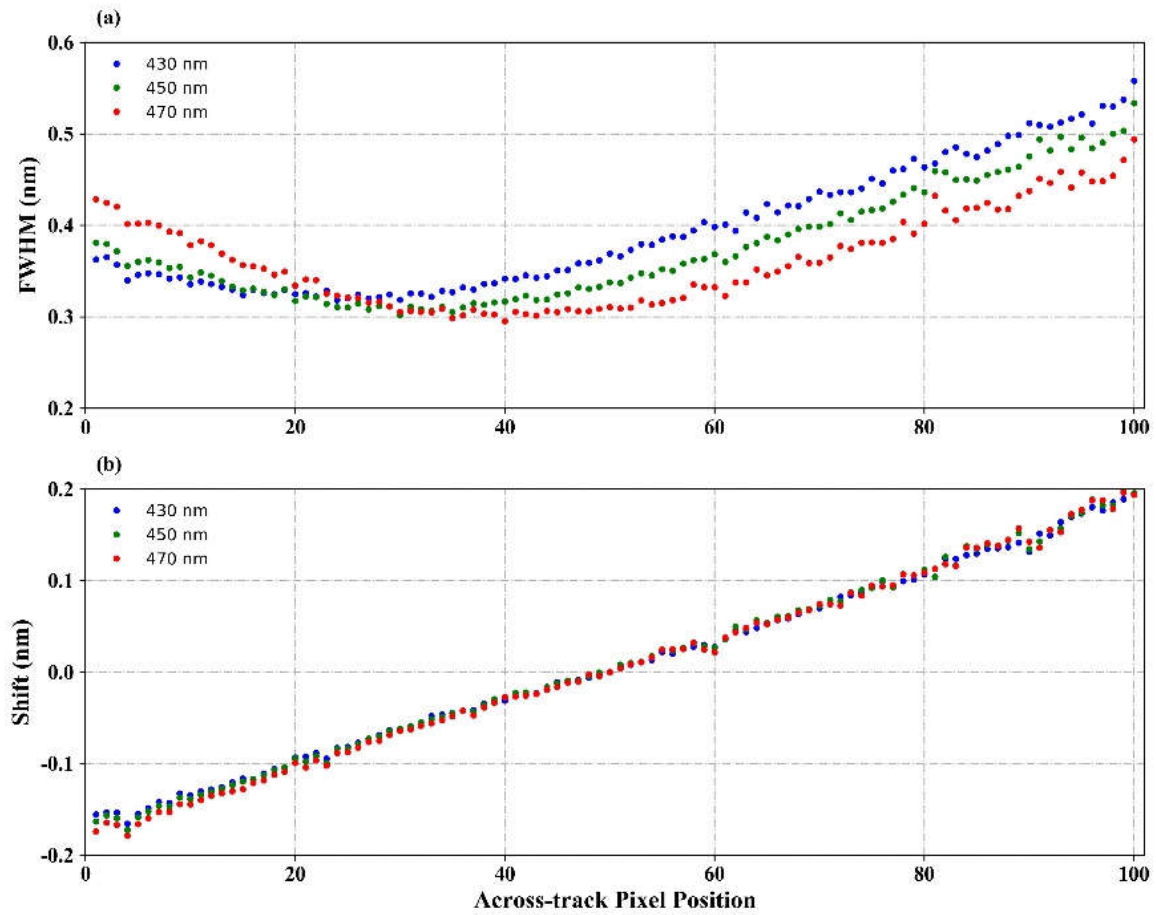


Figure 5. In-flight spectral calibration: (a) the spectral resolution (FWHM); (b) the spectral shift on different across-track position. Results at three wavelengths are plotted: blue for 430 nm, green for 450 nm and red for 470 nm.

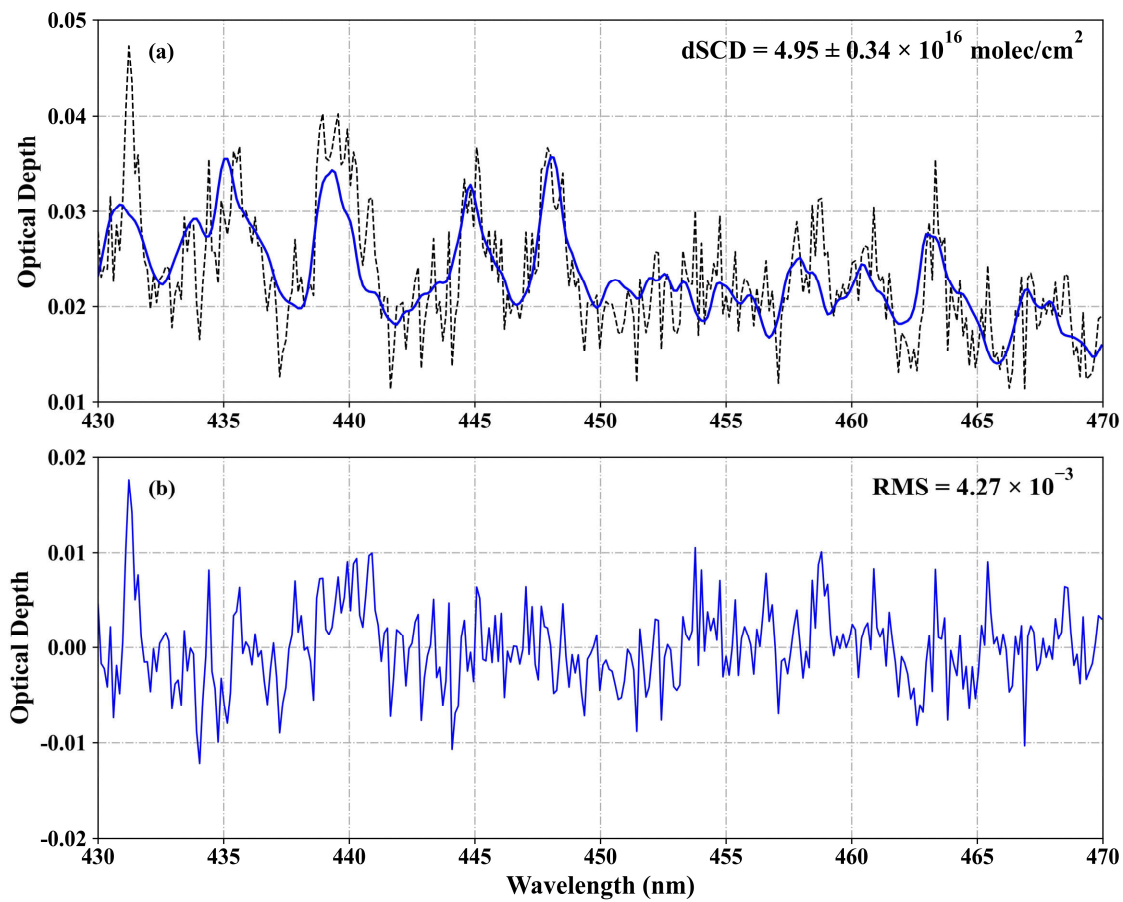


Figure 6. Sample DOAS fit result for NO₂: (a) observed (black dashed line) and fitted (blue line) optical depths from measured spectra; (b) the remaining residuals of DOAS fit.

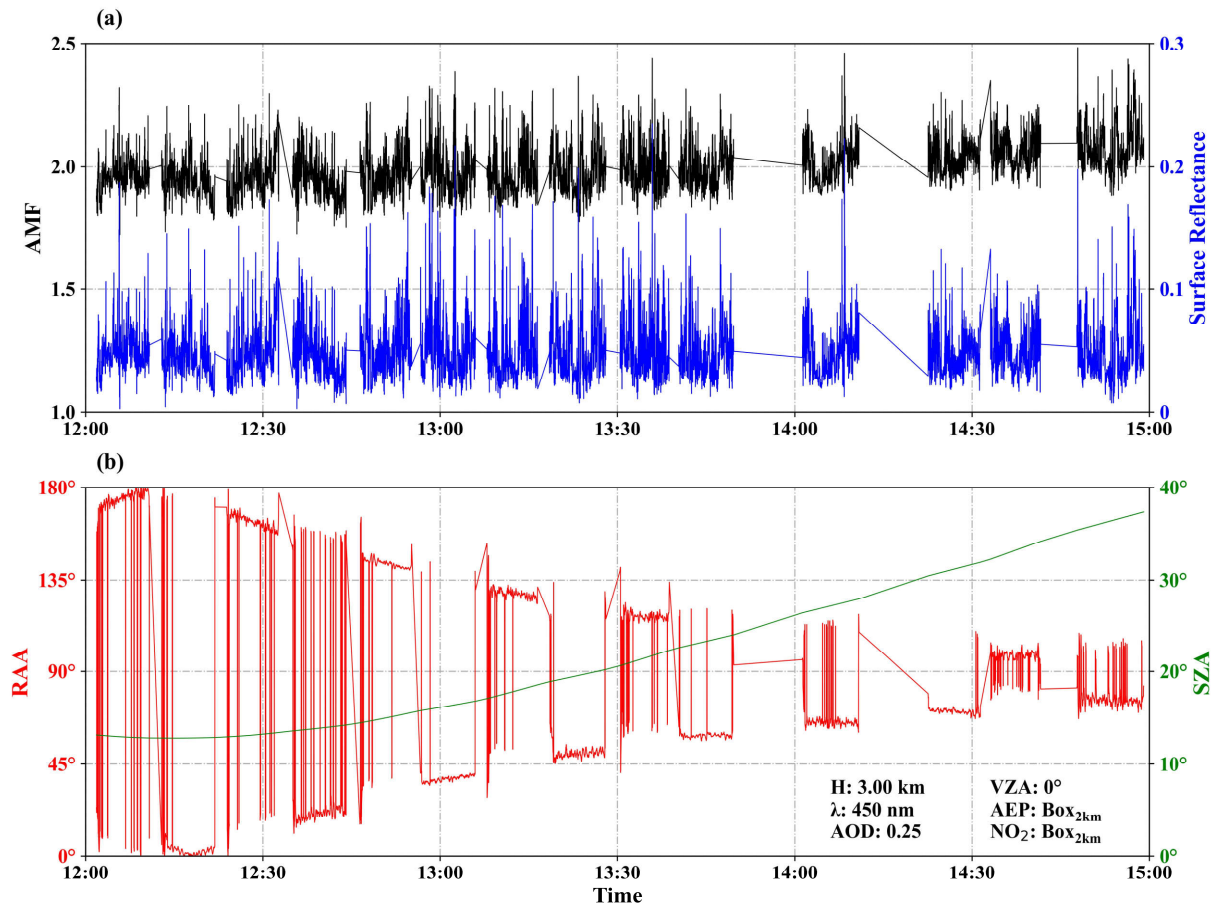


Figure 7. Time series of NO₂ AMF compared with (a) surface reflectance; (b) SZA and RAA for the research flight on 23 June 2018, computed with SCIATRAN model based on the RTM parameters from the UVHIS instrument. Only data of the nadir observations in each flight line are plotted.

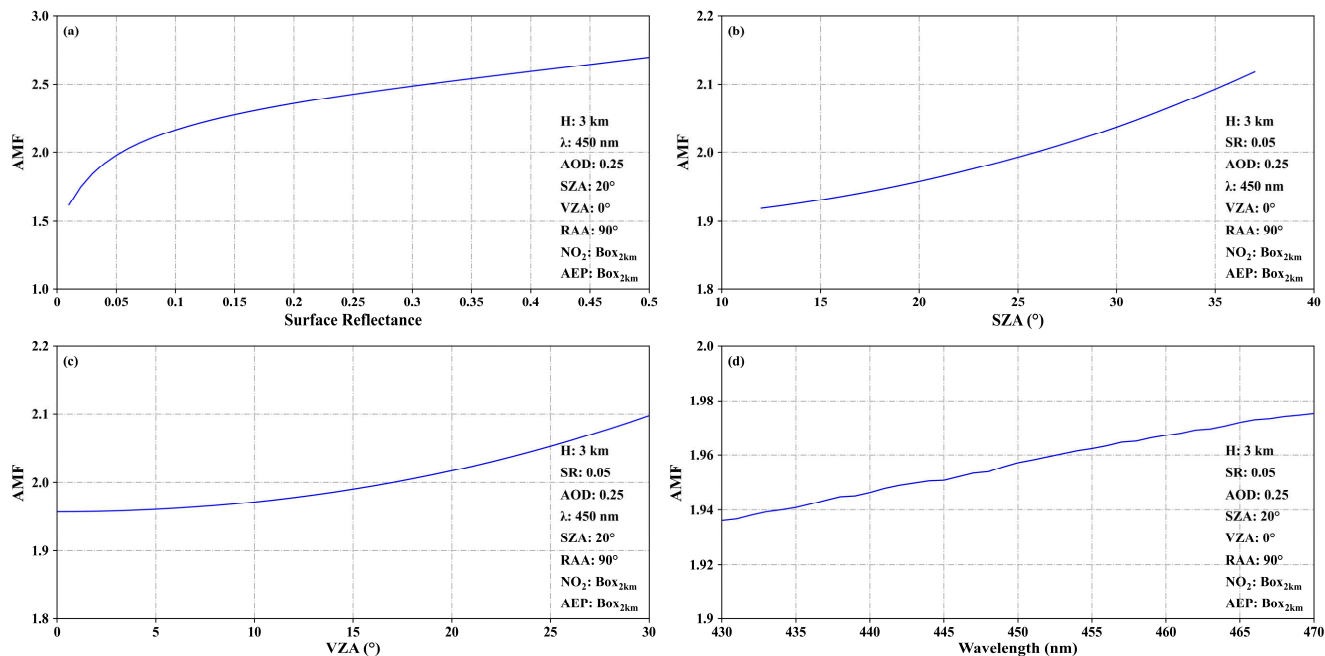
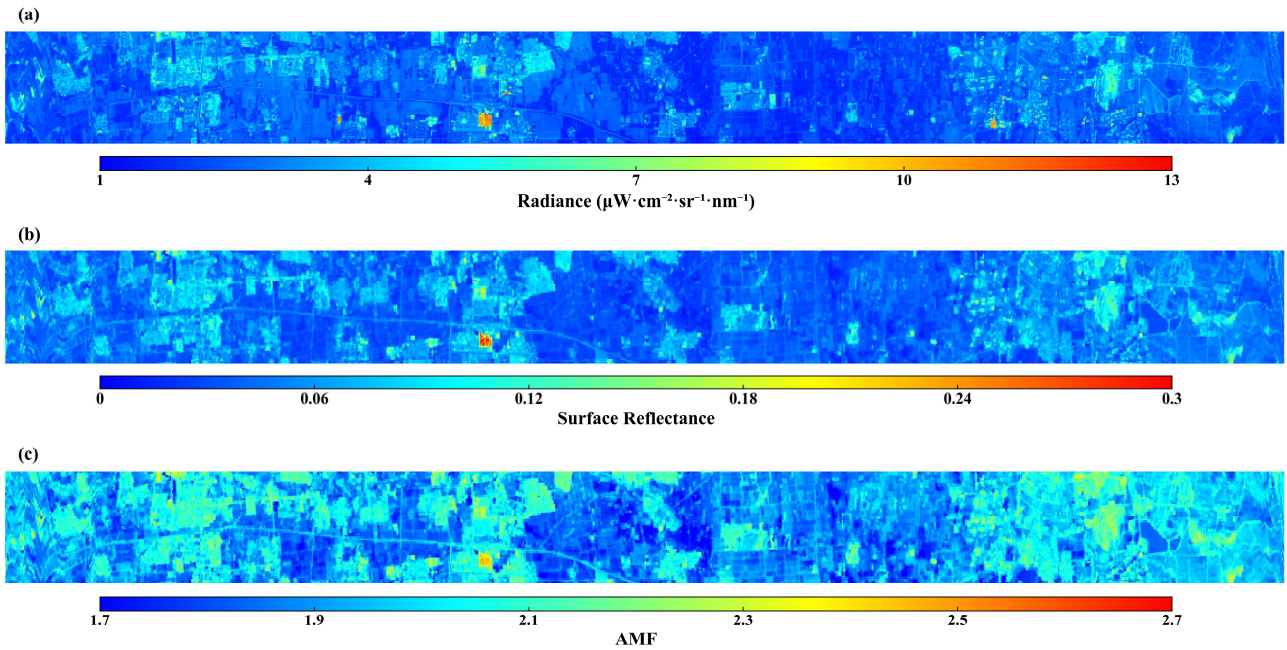


Figure 8. AMF dependence analysis results (a): on the surface reflectance; (b): on the SZAs; (c): on the VZAs; (d): on the wavelength.



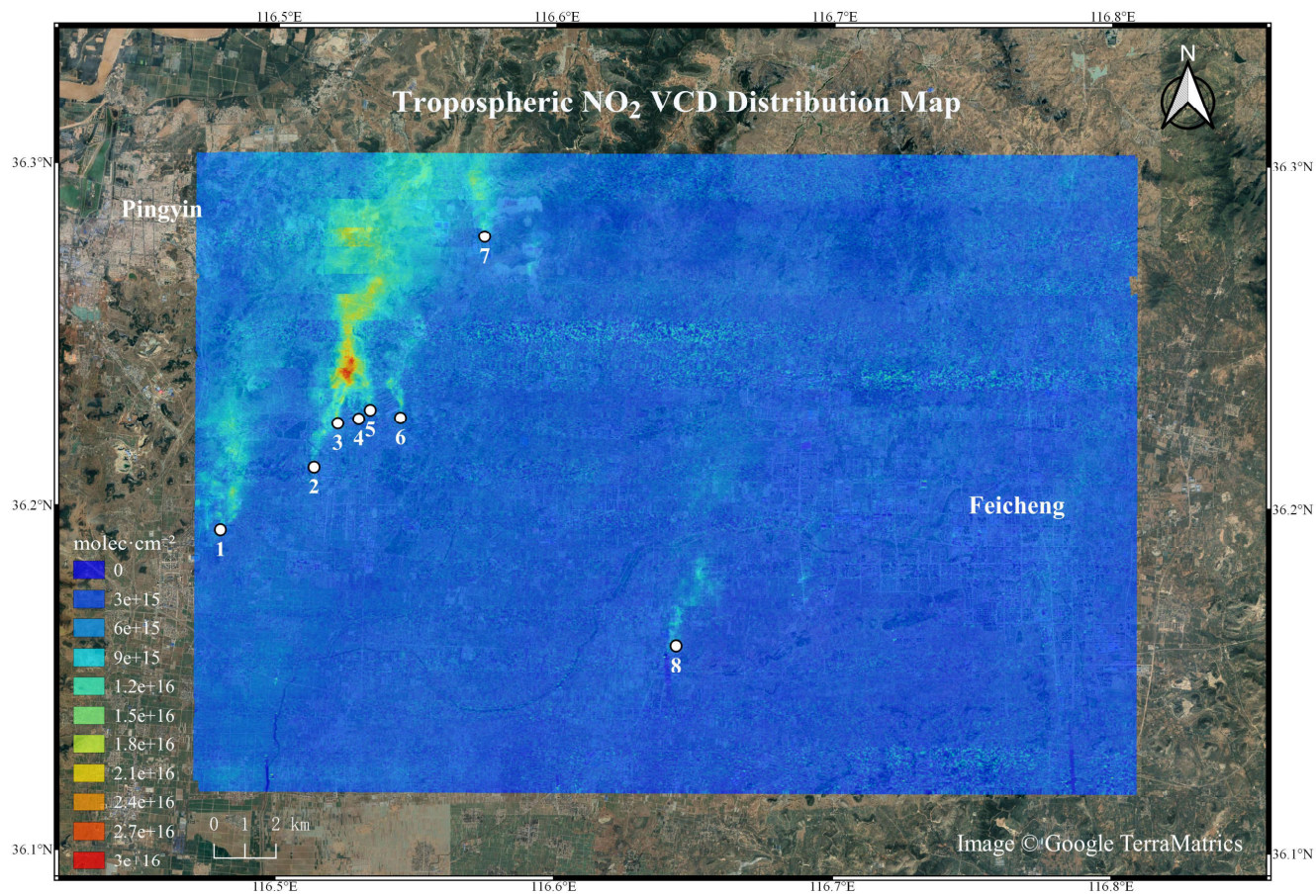
990

Figure 9. (a) UVHIS ~~Measured-measured~~ radiance; (b) Landsat 8 Surface reflectance; (c) computed AMFs, for one flight line of the Feicheng data set. A strong dependency of the AMF on the surface reflectance can be observed.

995

1000

1005



1010

Figure 10. Tropospheric NO₂ VCD map retrieved from UVHIS over Feicheng on 23 June 2018. The major contributing NO_2 NO_x emission sources are indicated by numbers 1 to 8.

1015

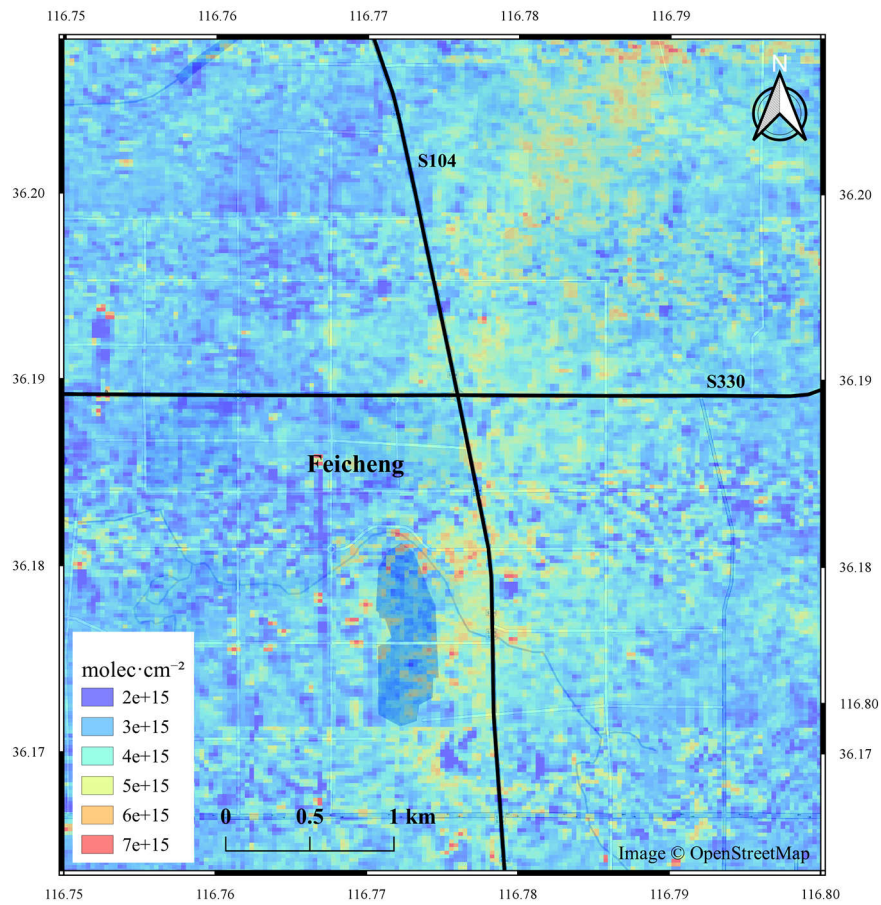


Figure 11. Enlargement of UVHIS NO₂ VCD map over Feicheng city with a ~~color~~ colour scale only extends to 7×10^{15} molec cm⁻². Two black lines in the map represent two truck roads that cross Feicheng city: S104, and S330.

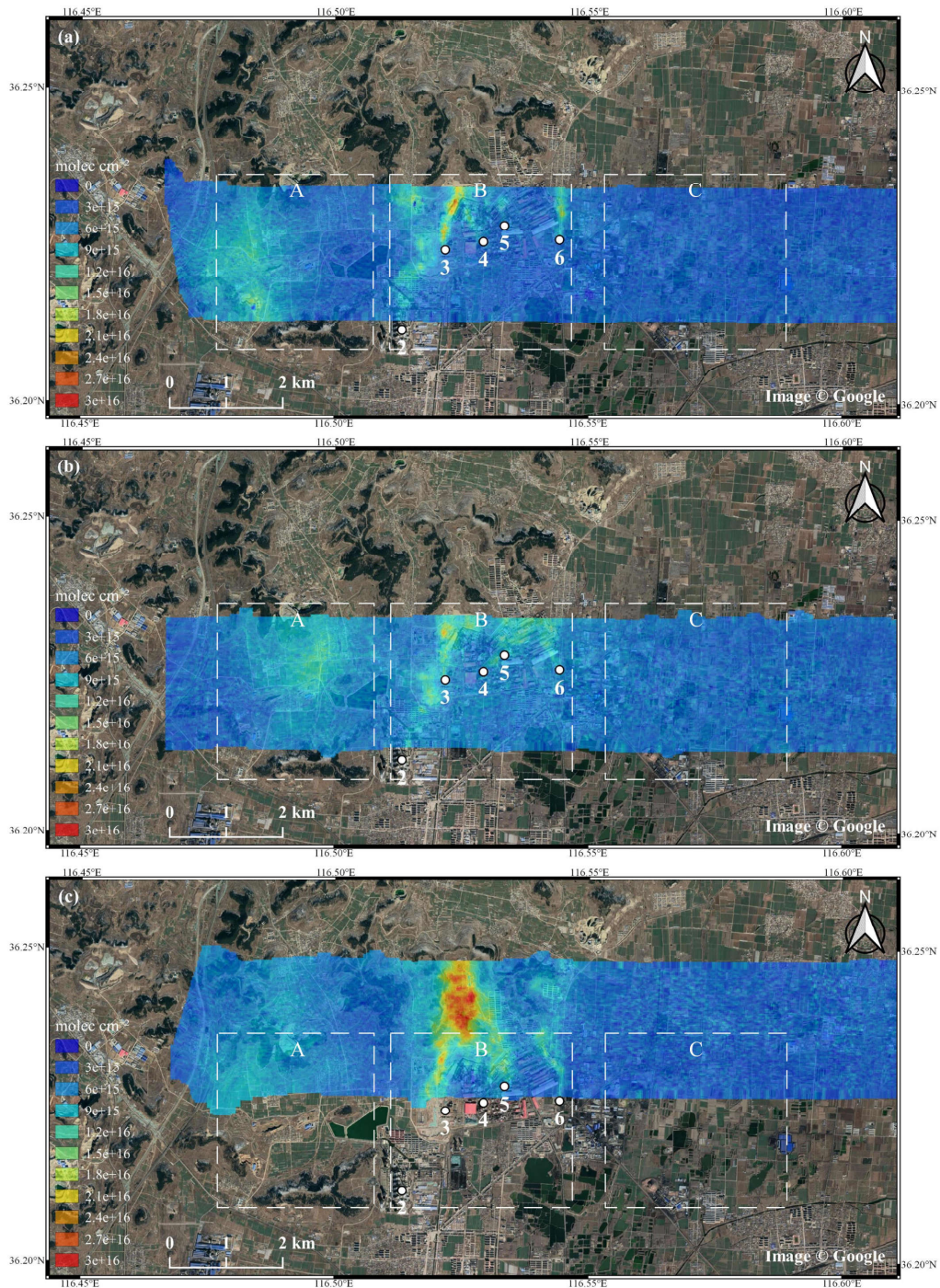


Figure 12. Three flight lines that pass through the steel factory, at local time 13:26 (a), 13:32 (c), and 14:57 (b). Panel (a) and (b) represent flight lines that cover the same area with a 1.5 hour-h time gap, panel (a) and (c) represent adjacent flight lines with a 6 minutes-min time gap.

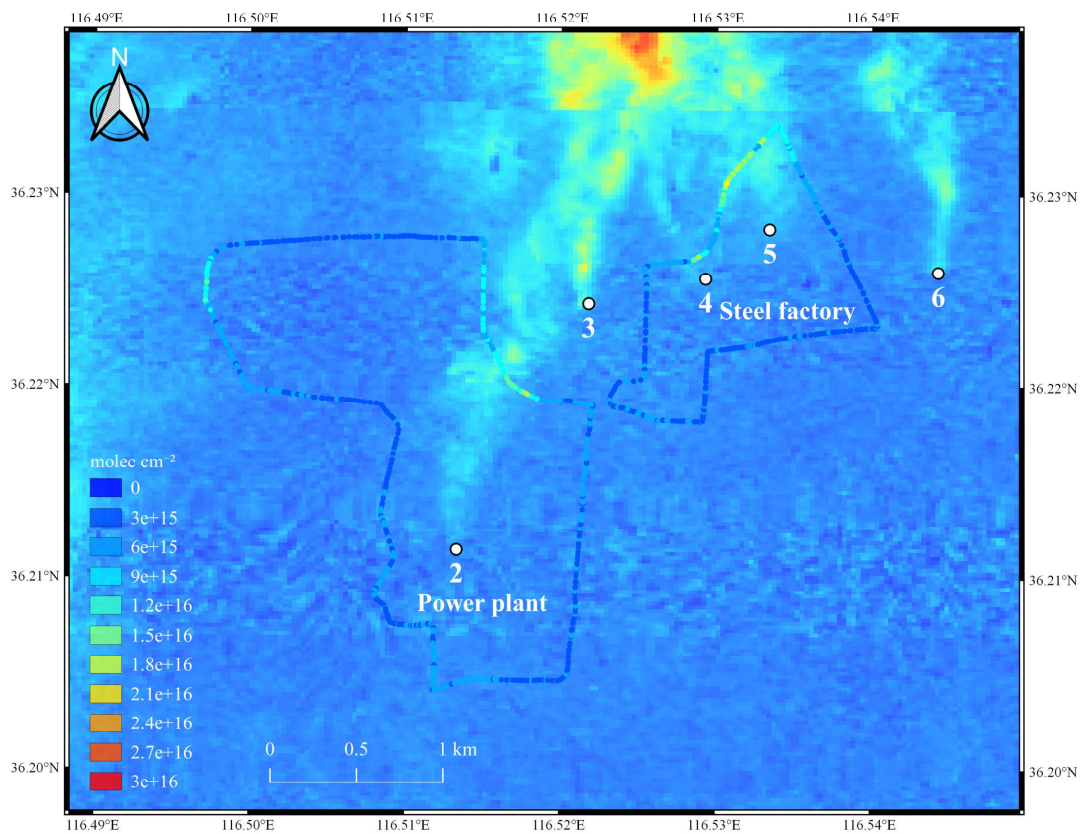


Figure 13. Overview of VCDs retrieved from ground-based mobile DOAS system (circle marks), and VCDs retrieved by UVHIS (background layer), measured on 23 June 2018.

1025

1030

1035

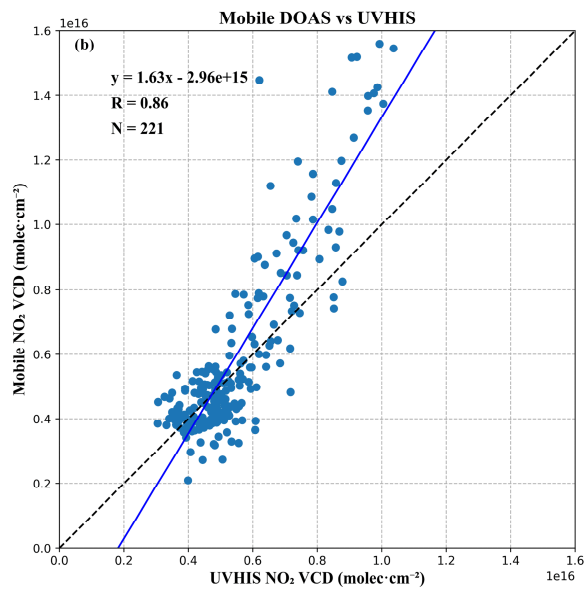
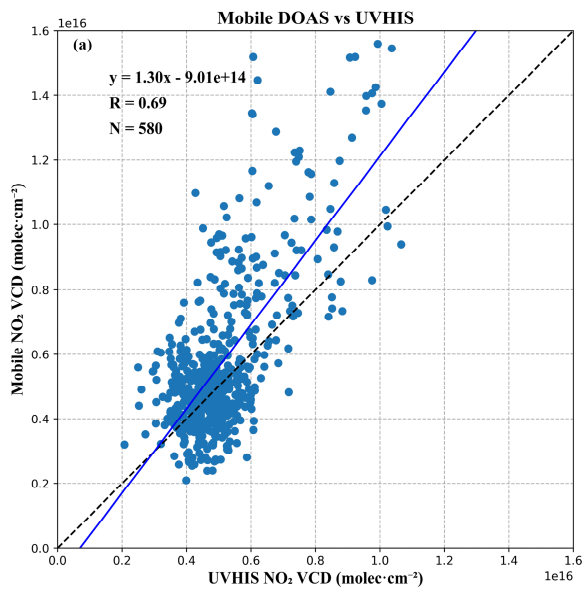


Figure 14. Scatter plot and linear regression analysis of the co-located NO₂ VCDs, retrieved from UVHIS and mobile DOAS system, (a) for all co-located measurements, with a time offset of 1 h, (b) for co-located measurements that only circled the steel factory, with a time offset of 15 min.

1040

1045